Title

Integrated Maneuvering Control For Automated Highway Systems Based On A Magnetic Reference/sensing System

Authors

Pham, Hung
Tomizuka, Masayoshi
Hedrick, J. Karl

Publication Date

1997

CALIFORNIA PATH PROGRAM
INSTITUTE OF TRANSPORTATION STUDIES
UNIVERSITY OF CALIFORNIA, BERKELEY

Integrated Maneuvering Control for Automated Highway Systems Based on a Magnetic Reference/Sensing System

Hung Pham, Masayoshi Tomizuka, J. Karl Hedrick
University of California, Berkeley

California PATH Research Report
UCB-ITS-PRR-97-28

This work was performed as part of the California PATH Program of the University of California, in cooperation with the State of California Business, Transportation, and Housing Agency, Department of Transportation; and the United States Department of Transportation, Federal Highway Administration.

July 1997

ISSN 1055-1425

MOU 88 - Final report

Integrated Maneuvering Control for Automated Highway Systems based on a Magnetic Reference/Sensing System

Hung Pham
Masayoshi Tomizuka (PI)
J. K. Hedrick (co-PI)

Partners for Advanced Transit and Highways (PATH)

Institute of Transportation Studies

University of California, Berkeley

Abstract

This report investigates the problem of regulation-level vehicle control for combined lateral and longitudinal maneuvers in an automated highway system (AHS) setting. Drawing from a number of earlier modeling results, a 26-state simulation model is proposed that offers the necessary level of fidelity for the study of combined vehicle maneuvers in typical freeway operations, while minimizing the level of complexity. Then, utilizing a set of simplified control models, it is shown that the coupling between the lateral and longitudinal dynamics can become appreciable during severe operations, such as those encountered during lane changes, emergency obstacle avoidance, or in inclement weather and road conditions. To corroborate this result, various coupled and de-coupled control strategies are used in vehicle simulations over a wide range of maneuvering profiles and operating conditions. In order to facilitate coupled control design for multiple input, multiple output (MIMO) systems with unseparable input nonlinearities, sufficient conditions are presented for the existence of an approximate (numerically obtained) control which guarantees bounded tracking.

In addition to controller design for individual agents, the issue of vehicle stability within an interconnected system is further investigated and a hybrid point-following, vehicle-following platooning strategy is proposed. It is shown that the hybrid scheme is superior to vehicle-following control with lead vehicle information because it: provides absolute ground-truth referencing; places much less demand on the radios; and is more robust, in string stable sense, to velocity estimation errors. Similarly, a dual-objective vehicle-following, lane-following lateral platooning strategy is also proposed.

Key words: IVHS, AHS, **AVCS,** Longitudinal control, Lateral control, String/Platoon stability.

Table of Contents

1 Executive summary

This report details work completed in the final phase (Phase 111) of the project titled, *Integrated Maneuvering Control for Automated Highway Systems Based on a Magnetic Referencing System.* The goal of which was to demonstrate the feasibility and effectiveness of utilizing magnetic markers embedded along the road center-line for both lateral and longitudinal control of vehicles for the Automated Highway Systems (AHS) concept.

The use of the magnetic marker referencing for independent lateral control has been successfully demonstrated by Peng and Tomizuka (1990) and Hessburg et. al. (1994). However, these studies disregard the possibility of dynamic and tire-force couplings arising from longitudinal vehicle motion. Similarly, longitudinal control studies conducted at PATH, Hedrick et. al. (1995), Xu and Ioannou (1994), and Sheikholeslam and Desoer (1990), have neglected the vehicle's lateral motions.

Yet, it is known that the motions are not completely independent. Consequently, unidirectional control designs invite unforeseen dangers arising from its neglect of the coupling dynamics. Moreover, the referencing systems utilized in these aforementioned studies were often mutually exclusive, with little thought given to possible benefits derived from complementary coverage. Thus, in an effort to redress some of these shortcomings, this study takes a unified approach towards the modeling, control, and sensing of vehicles for AHS application.

The study is framed within the proposed AHS architecture favored by the California Partners for Advanced Transit and Highways (PATH), whereby intelligent vehicles are assigned to dedicated lanes by a decentralized roadside coordinator. This coordinator "suggests" a desired velocity; the vehicle controller is charged with following the reference velocity and maintaining the lateral position. Magnetic markers embedded in the road provide geometry, and lateral and longitudinal position reference. In addition,

relative vehicle spacing information can be obtained via a radar or vision referencing system. Finally, onboard inertial sensors are utilized to provide a measure of the vehicle's absolute motion.

Within this context, the following points are explored and conclusions advanced. In particular, effort is made to quantify the lateral and longitudinal couplings through a simulation study utilizing a full 26-state vehicle model that details the vehicle sprung mass motion in all six degrees of freedom. To complement the numerical study, an analysis of the dynamics of a reduced-order model is also presented. From these results, it is concluded that the coupling becomes apparent even at moderate lateral and longitudinal maneuvers (*i.e.* < 2 m/s^2) under conditions of low road friction. The performance of the independent lateral and longitudinal controllers is shown to degrade significantly in the presence of this coupling.

In addition to the coupling investigation, an alternative platooning strategy is also proposed. Departing from the more traditional platooning schemes, the proposed hybrid policy, which utilizes radar and magnetic marker as reference, combines elements from both constant spacing vehicle-following and point-following strategies. The point-following portion guarantees stability of the entire platoon by providing absolute "ground-truth" referencing, while the vehicle-following portion allows for safe, close-packing of the vehicles. In order to facilitate the analysis of the sampled-data system, sufficient conditions for the stability of interconnected system are also presented.

In a similar vein, both radar and marker referencing systems are exploited in a dual-objective lateral platooning strategy. The radar provides a heading angle reference which damps the vehicle's internal yaw dynamics. At the same time, the markers ensures lateral string stability by tying each vehicle to the lane center. Aside from the performance guarantees, it is also argued that the dual-objective strategy is more robust to sensing system failures since the vehicles remain operable (albeit, sub-optimally) under either heading angle or marker-following control.

2 Vehicle Model

2.1 Introduction

A crucial first step in model-based controller design is the development of a mathematically tractable model which accurately describes plant behavior within the operating range of interest. In early longitudinal control studies, vehicles models assumed simple second-order chassis dynamics (Bender, 1973). Later refinements increased model fidelity by including fifth-order steady-state engine, transmission, and drive-train dynamics (McMahon et. al., 1990). However, dynamics in the lateral, vertical, and rotational degrees of freedom were still largely ignored.

Conversely, lateral control models often neglected engine dynamics and, instead, focused on a detailed description of the sprung mass and the tire/road interaction (Peng and Tomizuka, 1990). The above-mentioned lateral, vertical, and rotational motions were described, but little effort was made to explain the mechanisms of driving or braking torque generation. Neither were there any discussions concerning the kinematics or tire force couplings between the lateral and longitudinal dynamics.

Thus, in order to advance a comprehensive combined longitudinal and lateral control study, it is necessary to integrate the salient features of the separate longitudinal and lateral models into a single model. Such a model becomes a central part of the design process as it can be used in computer simulations to test the validity and efficacy of the controller before actual implementation on the test vehicle. The simulation model can also be used to modify controller design in subsequent iterations once the subtleties of vehicle closed-loop behavior are better understood from initial field tests.

The combined model described in the following sections includes six degrees of freedom for the vehicle sprung mass, dynamics of engine and manifold, a torque

converter, as well as tire and suspension dynamics. The inputs to the front-wheel driven, front-wheel steered model are the throttle and steering angles and brake torque. The model parameters are adapted for the 1986 3.8L V-6 GM Pontiac vehicle used for combined control experiments at UC Berkeley's Richmond Field testing facilities. It should be noted from the outset that there are no novel modeling approaches presented. Rather, this chapter merely represents an effort to amass previous modeling results from a variety of sources into a single, comprehensive collection.

Also, note the use of the word, "adapted." This is due to the fact that a complete set of parameters for the Pontiac vehicle is not currently available. Instead, we rely on three separate parameter sets: the 1990 Ford Lincoln Towncar (longitudinal); the 1988 Toyota Celica (lateral); and the Pontiac. A table of parameter values and their respective origins is available in Appendix A. As a separate element, the power capabilities of the longitudinal model (Towncar) has been validated in field tests conducted under the UCB-PATH program (Hedrick et. al., 1992). Likewise, the handling performance of the lateral model (Celica) has also been validated in field tests (Peng et. al., 1992). Consequently, by judicious use and a careful scaling of the parameters, we expect that the hybrid-parameter model's behavior should closely follow the behavior of the actual test vehicle.

2.2 Complex simulation model

2.2.1 Sprung mass submodel

Following is a listing of the nomenclature found in the sprung mass submodel, which includes a description of the vehicle kinematics along with the external forces and moments. The sprung mass schematic is given in Figure 2.1.

The nomenclature adhered to in this section are given by:

x, V_x	longitudinal position, velocity	
y, V_y	lateral position, velocity	
z, V_z	vertical position, velocity	
ϕ	roll angle	
θ	pitch angle	
ψ	yaw angle	
β	vehicle side slip angle	
χ	vehicle velocity angle	
$C_x(C_y)$	longitudinal (lateral) wind drag coefficient	
h_2	vertical distance from c.g. to roll center	
$h_4(h_5)$	vertical (longitudinal) distance from c.g. to pitch center	
$I_{x(y)(z)}$	vehicle principle moment of inertia about $-x$ $(-y)(-z)$ axis	
$l_f(l_r)$	longitudinal distance from c.g. to front (rear) axle	
m	vehicle mass	
$s_f(s_r)$	track of front (rear) axle	
F_{roll}	total rolling resistance of tires	
$F_{A_i(B_i)(P_i)}$	net longitudinal (lateral) (normal) force from i^{th} tire	$i = 1,..,4$
$M_{x(y)(z)}$	moment about $-x$ $(-y)$ $(-z)$axis	
$F_{x_i(y_i)}$	traction (cornering) force on i^{th} tire	$i = 1,..,4$
δ_f	steering angle of front tires	

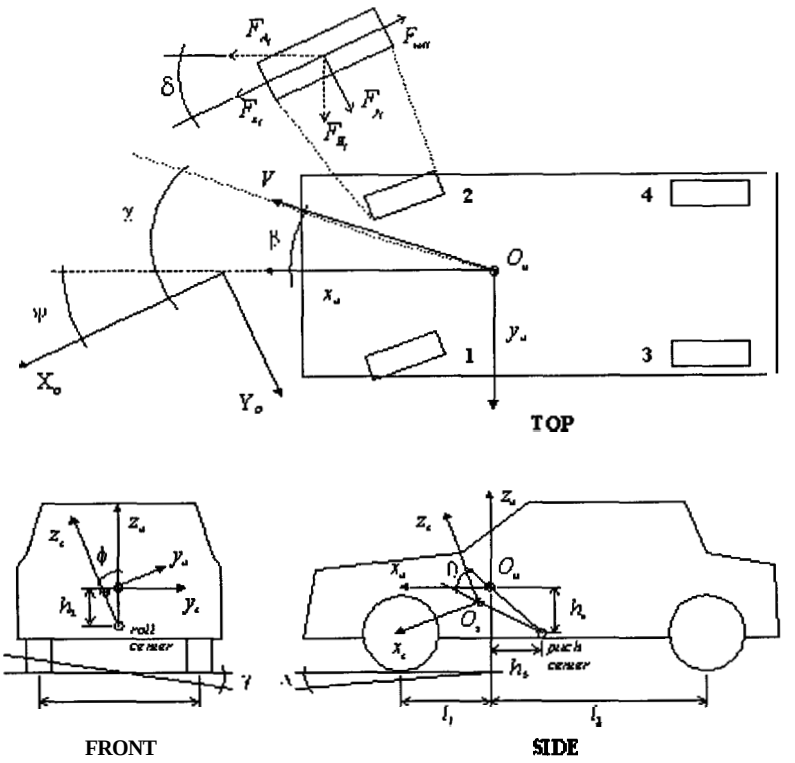

Figure 2.1: Schematic of spring mass submodel.

2.2.1a Kinematics

The motion of a particle along a curve, $C(\cdot):\Re \to \Re^3$, can be resolved into its normal, $\mathbf{n} \in \Re^3$, tangential, $\mathbf{t} \in \Re^3$, and binormal components, $\mathbf{b} \in \Re^3$. These directions are the well-known "intrinsic coordinates" and provide a convenient starting point for the derivation of the chassis equations of motion. However, as the external forces enter the vehicle through the tires, it is more apt to **frame** the *final* form of the equations in the coordinates fixed onto the vehicle ***unsprung*** *mass* (*i.e.* the frame and tires). All told, we rely on a total of three sets of rotating and translating coordinate axes (Fig 2.2) to derive the sprung mass equations: *Otnb*, the above-mentioned intrinsic coordinates; $O_u x_u y_u z_u$, the unsprung mass coordinates, and $O_s x_s y_s z_s$, ***sprung*** *mass* coordinates (***ie.*** vehicle center of mass).

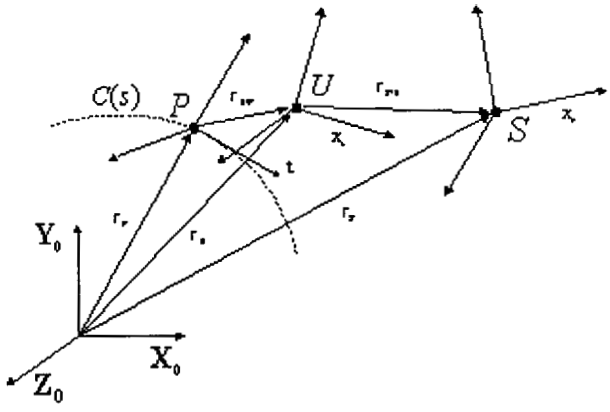

Figure 2.2: Motion of vehicle center of mass (*S*).

, $\ddot{\mathbf{r}}_S$, sprung mass acceleration:

Referring to Figure 2.2, let U be unsprung mass center and let S be the sprung mass center. Let $\mathbf{r}_U$ be the vector from the origin to U and let $\mathbf{r}_{S/U}$ be the vector from U to S. The acceleration of the sprung mass, *with respect to the unsprung coordinates*, can be found from

$$ {}_u\ddot{\mathbf{r}}_S = {}_u\ddot{\mathbf{r}}_U + {}_u\ddot{\mathbf{r}}_{S/U} \tag{2.1} $$

where the left-hand subscript "u" denotes differentiation of the vector with respect to the rotating reference frame $O_u x_u y_u z_u$. The following discussion centers on finding expressions for the right side of (2.1).

For planar motion, the angular velocity of the frame *Otnb*, expressed with respect to its coordinates, is

$$ {}_i\boldsymbol{\omega}_O = \dot{s}\kappa\, b = \begin{bmatrix} 0 & 0 & \dot{\chi} \end{bmatrix}^{\mathrm{T}} \tag{2.2} $$

where $\dot{s}$ is the speed along the path, $C(s)$, and κ is the path curvature. We call $\dot{\chi}$ the velocity angle. With respect to this path, the sprung mass is perturbed by small superelavation (γ), gradient **(A),** and sideslip (β) angles (Fig 2.1). The angular velocity of *Otnb* relative to $O_u x_u y_u z_u$ **,** then, is given by

$$ {}_i\boldsymbol{\omega}_{O_u/O} = \begin{bmatrix} \dot{\gamma} & \dot{\Delta} & -\dot{\beta} \end{bmatrix}^{\mathrm{T}} \tag{2.3} $$

with the corresponding rotation

$$ {}_u\Theta_{in} \approx \begin{bmatrix} 1 & \beta & -\Delta \\ -\beta & 1 & \gamma \\ \Delta & -\gamma & 1 \end{bmatrix} \tag{2.4} $$

where the $\approx$ in (2.4) indicates the truncation of second-order terms.

Combining (2.2-4), the angular velocity of the unsprung mass, expressed with respect to the unsprung coordinates, can be written as

$$ {}_u\omega_{O_u} = {}_u\Theta_i \left\{ {}_i\omega_{O_u/O} + {}_i\omega_{O_i} \right\} \tag{2.5} $$

$$ = \begin{bmatrix} \dot{\gamma} + \beta\dot{\Delta} - \Delta\dot{\psi} \\ -\beta\dot{\gamma} + \dot{\Delta} + \gamma\dot{\psi} \\ \dot{\psi} \end{bmatrix} $$

where $\dot{\psi} = \Delta\dot{\gamma} - \gamma\dot{\Delta} + \dot{\chi} - \dot{\beta}$ is the vehicle yaw rate.

The velocity of the unsprung mass, with respect to its body-fixed coordinates, is described as

$$ {}_u\dot{\mathbf{r}}_U = \begin{bmatrix} V_x & V_y & 0 \end{bmatrix}^{\mathrm{T}} \tag{2.6} $$

where the z-th component of the velocity, resulting from the tire deflection rate, is assumed to be negligible. Then, following the rules of vector differentiation with respect to a moving reference frame, the acceleration of U becomes

$$ \frac{d}{dt}\left({}_u\dot{\mathbf{r}}_U \right) = \frac{\partial}{\partial t}\left({}_u\dot{\mathbf{r}}_U \right) + {}_u\omega_{O_u} \times {}_u\dot{\mathbf{r}}_U \tag{2.7} $$

$$ = \begin{bmatrix} \dot{V}_x \\ \dot{V}_y \\ 0 \end{bmatrix} + \begin{bmatrix} -V_y\dot{\psi} \\ V_x\dot{\psi} \\ V_y\left\{ \dot{\gamma} + \beta\dot{\Delta} - \Delta\dot{\psi} \right\} - V_x\left\{ -\beta\dot{\gamma} + \dot{\Delta} + \gamma\dot{\psi} \right\} \end{bmatrix} $$

Moreover, due to the presence of the suspension, the sprung mass undergoes roll (ϕ), pitch (e), and vertical (z), motions relative to the unsprung mass. From simple geometry, the relative position vector from U to S is given by

$$ {}_u\mathbf{r}_{S/U} = \begin{bmatrix} h_4\theta & -h_2\phi & z - h_5\theta \end{bmatrix}^{\mathrm{T}} \tag{2.8} $$

Consequently the relative sprung mass acceleration, with respect to $O_u x_u y_u z_u$, can be found from

$$ {}_u\ddot{\mathbf{r}}_{S/U} = \frac{\partial^2}{\partial t^2}\left({}_u\mathbf{r}_{S/U}\right) + 2\,{}_u\omega_{O_u} \times \frac{\partial}{\partial t}\left({}_u\mathbf{r}_{S/U}\right) + {}_u\dot{\omega}_{O_u} \times {}_u\mathbf{r}_{S/U} + {}_u\omega_{O_u} \times {}_u\omega_{O_u} \times {}_u\mathbf{r}_{S/P} \tag{2.9} $$

$$ \approx \begin{bmatrix} h_2\phi\ddot{\psi} + 2h_2\dot{\phi}\dot{\psi} + h_4\ddot{\theta} + 2(\mathbf{z} - h_5\theta)\ddot{\Delta} + \left(\mathbf{Z} - h_5\dot{\theta}\right)\dot{\Delta} \\ -h_2\ddot{\phi} + h_4\theta\ddot{\psi} + 2h_4\dot{\theta}\dot{\psi} + (\mathbf{z} - h_5\theta)\ddot{\gamma} - 2\left(\dot{z} - h_5\dot{\theta}\right)\dot{\gamma} \\ -h_2\phi\ddot{\gamma} - 2h_2\dot{\phi}\dot{\gamma} - h_4\theta\ddot{\Delta} - 2h_4\dot{\theta}\dot{\Delta} + \ddot{z} - h_5\ddot{\theta} \end{bmatrix} $$

where all the second-order terms in $(z, \theta, \phi, \mathbf{A}, \beta, \gamma,)$ and third-order terms involving their derivatives have been neglected. Finally, the total acceleration of the sprung mass, ${}_u\ddot{\mathbf{r}}_S$, can be found from **(2.**1), **(2.7)** and **(2.9).**

${}_s\dot{\omega}_{O_s}$,sprung mass angular acceleration:

The sprung mass angular velocity can be found as the sum of the unsprung mass angular velocity **(2.5)** and the relative angular velocity between the two masses, *i.e.*

$$ {}_s\omega_{O_s} = {}_s\Theta_u\left\{{}_u\omega_{O_u} + {}_u\omega_{O_s/O_u}\right\} \tag{2.10} $$

where ${}_s\Theta_u$ is the rotation between $O_u x_u y_u z_u \rightarrow O_s x_s y_s z_s$ and is given by

$$ {}_s\Theta_u \approx \begin{bmatrix} 1 & 0 & -\theta \\ 0 & 1 & \phi \\ \theta & -\phi & 1 \end{bmatrix} \tag{2.11} $$

Clearly, ${}_u\omega_{O_s/O_u} = \begin{bmatrix} \dot{\phi} & \dot{\theta} & 0 \end{bmatrix}^{\mathrm{T}}$. Hence, from **(2.5)** and (2.10), we have that

$$ {}_s\omega_{O_s} = {}_s\Theta_u\left\{{}_u\omega_{O_s/O_u} + {}_u\omega_{O_u}\right\} = \begin{bmatrix} \dot{\phi} + \dot{\gamma} + \beta\dot{\Delta} - \{\Delta + \theta\}\dot{\psi} \\ \dot{\theta} - \beta\dot{\gamma} + \dot{\Delta} + \{\gamma + \phi\}\dot{\psi} \\ \theta\{\dot{\phi} + \dot{\gamma}\} - \phi\{\dot{\theta} + \dot{\Delta}\} + \dot{\psi} \end{bmatrix} \tag{2.12} $$

2.2.1b External forces and moments

From the geometry of the vehicle (Fig 2.1), the external forces along the unsprung mass coordinates are found as

$$F_{A_i} = F_{x_i} - \delta_i \cdot F_{y_i} \qquad i = 1,..,4 \tag{2.13}$$

$$F_{B_i} = F_{y_i} - \delta_i \cdot F_{x_i} \qquad i = 1,..,4$$

$$F_{P_i} = F_{spring_i} + F_{damp_i} \qquad i = 1,..,4$$

where F_x and F_y are calculated from the tire model **(section 2.2.2)** and F_{spring} and F_{damp} are calculated from the suspension model **(section 2.2.3).** Observe that for a front-wheel steered vehicle, $\delta_4 = 0$.

Also from geometry, the moments about the unsprung mass are found as

$$M_x = \left\{\frac{s_f}{2} + h_2\phi\right\}F_{P_1} + \left\{\frac{s_r}{2} + h_2\phi\right\}F_{P_3} - \left\{\frac{s_f}{2} - h_2\phi\right\}F_{P_2} - \left\{\frac{s_r}{2} - h_2\phi\right\}F_{P_4} \tag{2.14}$$

$$-\{z - h_5\theta\}\sum_{i=1}^{4} F_{B_i}$$

$$M_y = \{l_r + h_4\theta\}\{F_{P_3} + F_{P_4}\} - \{l_f - h_4\theta\}\{F_{P_1} + F_{P_2}\} - \{z - h_5\theta\}\sum_{i=1}^{4} F_{A_i}$$

$$M_z = \{l_f - h_4\theta\}\{F_{B_1} + F_{B_2}\} - \{l_r - h_4\theta\}\{F_{B_3} + F_{B_4}\} - \left\{\frac{s_f}{2} + h_2\phi\right\}F_{A_1}$$

$$-\left\{\frac{s_r}{2} + h_2\phi\right\}F_{A_3} + \left\{\frac{s_f}{2} - h_2\phi\right\}F_{A_2} + \left\{\frac{s_r}{2} - h_2\phi\right\}F_{A_4}$$

2.2.1c Equations of motion

The results of **secs. 2.2.1a-b** can be combined to yield the equations of motion for the vehicle sprung mass. Note that the external moments in (2.14) are with respect to the ***unsprung*** coordinates, but that the moment of inertia values are about the ***sprung*** mass principle axes. Consequently, we must apply Euler's equations for rigid body motion to

obtain the dynamic equations governing the angular motion about the sprung mass principle axes, i e.

$$I_x\dot{\omega}_x - \{I_y - I_z\}\omega_y\omega_z = M_{x_s}$$
$$I_y\dot{\omega}_y - \{I_z - I_x\}\omega_z\omega_x = M_{y_s} \qquad (2.15)$$
$$I_z\dot{\omega}_z - \{I_x - I_y\}\omega_x\omega_y = M_{z_s}$$

Hence, from (2.11), (2.12) and (2.15), the sprung mass rotational equations of motion can be written as

$$I_x\left[\ddot{\phi} + \ddot{\gamma} + \beta\ddot{\Delta} + \dot{\beta}\dot{\Delta} - \{\Delta + \theta\}\ddot{\psi} - \{\dot{\Delta} + \dot{\theta}\}\dot{\psi}\right] - \{I_y - I_z\}\{\dot{\Delta} + \dot{\theta}\}\dot{\psi} = M_x - \theta M_z \qquad (2.16)$$

$$I_y\left[\ddot{\theta} - \text{pi}; - \dot{\beta}\dot{\gamma} + \text{A} + \{\gamma + +\}@ - \{\dot{\gamma} + \dot{\phi}\}\dot{\psi}\right] - \{I_z - I_x\}\{\dot{\gamma} + \dot{\phi}\}\dot{\psi} = M_y + \phi M_z$$

$$I_z\left[\text{e}\{\dot{\gamma} + \dot{\phi}\} + \theta\{\ddot{\gamma} + \ddot{\phi}\} - \dot{\phi}\{\dot{\Delta} + \dot{\theta}\} - \phi\{\ddot{\Delta} + \ddot{\theta}\} + \ddot{\psi}\right] - \{I_x - I_y\}\{\dot{\gamma} + \dot{\phi}\}\{\dot{\Delta} + \dot{\theta}\} =$$
$$\theta M_x - \phi M_y + M_z$$

. where the moments are found from (2.14).

The translational equations of motion are

$$m\left[\dot{V}_x - V_y\dot{\psi} + h_2\phi\ddot{\psi} + 2h_2\dot{\phi}\dot{\psi} + h_4\ddot{\theta} + 2\{z - h_5\theta\}\ddot{\Delta} + \{\dot{z} - h_5\dot{\theta}\}\dot{\Delta}\right] = \qquad (2.17)$$
$$\sum_{i=1}^{4} F_{A_i} - C_x V_x^2 - F_{roll} + \Delta mg$$
$$m\left[\dot{V}_x + V_x\dot{\psi} - h_2\ddot{\phi} + h_4\theta\ddot{\psi} + 2h_4\dot{\theta}\dot{\psi} + \{z - h_5\theta\}\ddot{\gamma} - 2\{\dot{z} - h_5\dot{\theta}\}\dot{\gamma}\right] =$$
$$\sum_{i=1}^{4} F_{B_i} - C_y V_y^2 - \gamma mg$$
$$m\left[V_y\{\dot{\gamma} + \beta\dot{\Delta} - \Delta\dot{\psi}\} - V_x\{-\beta\dot{\gamma} + \dot{\Delta} + \gamma\dot{\psi}\} - h_2\phi\ddot{\gamma} - 2h_2\dot{\phi}\dot{\gamma} - h_4\theta\ddot{\Delta} - 2h_4\dot{\theta}\dot{\Delta} + \ddot{z} - h_5\ddot{\theta}\right] =$$
$$\sum_{i=1}^{4} F_{P_i} - mg$$

where $C\_V\_^2$ are the wind drag terms and F_{roll} is a fictitious quantity, called the rolling resistance, used to describe the energy lost during tire deformation (Gillespie, 1992). Its value differs with different tires and pressures, but is usually taken to be independent of velocity.

2.2.2 Suspension submodel

The automotive suspension is a crucial element in vehicle handling and road-holding. The term "handling" is a qualitative description of the lateral response of the vehicle, while "road-holding," refers to the tire's ability to grip the road. It is known that large tire deflection results in relatively poor traction, braking, and cornering. However, the suspension acts to reduce tire deflection by absorbing energy that would otherwise be transmitted to the tires; thus, road-holding is improved. On the downside, the cost of an over-compliant suspension comes as increased roll and pitch motions of the sprung mass, which decreases handling performance. Hence, a good suspension design provides a satisfactory compromise between the two extremes.

Most mathematical models of independent suspensions assume a two degree of freedom quarter car model (Butsuen, 1989). It has been shown, though, that for mid-sized passenger cars, the sprung mass natural frequency is around 1 *hz*, whereas the unsprung mass natural frequency is around 10 *hz* (Rajamani, 1993). For our level of fidelity, therefore, we can neglect the motion of the unsprung mass. Therefore, the suspension model adopted here is a simple one degree of freedom model with shock absorber and hardening spring (Peng, 1992).

Neglecting the small coupling terms, the suspension forces can be completely determined by the local motion at each wheel (Tseng, 1993). Let e_i be the deflection at the i^{th} suspension joint.

$$e_{1,2} = z_0 - z + h_5\theta + l_f\theta \pm \frac{s_f}{2}\phi \tag{2.18}$$

$$e_{3,4} = z_0 - z + h_5\theta - l_r\theta \mp \frac{s_r}{2}\phi$$

where z_0 is the nominal height. The spring force is then

$$F_{spring_i} = C_1\left\{e_i + C_2 e_i^3\right\} \tag{2.19}$$

and the damping force is

$$F_{damp_i} = D_1 \dot{e}_i \qquad |\dot{e}_i| < \overline{w}$$
$$= sign(\dot{e}_i)\{D_1 \overline{w} + D_2(|\dot{e}_i| - W)\} \qquad |\dot{e}_i| \geq W \tag{2.20}$$

2.2.3 Tire submodel

Following Peng (1992), we utilize the Bakker-Pacjeka model to calculate the traction and cornering forces resulting from the road-tire interaction. The use of this empirical curve-fit allows a clear relationship between the geometry of the interaction and the generated forces. A further incentive for the use of the model comes from the fact that Peng has made available a set of test data from experiments using a Yokohama P205/60R1487H tire. The availability of such data fitted to the Bakker-Pacjeka model enables us to accurately predict the behavior of the specific tire.

Tire related variables are defined as follow:

λ_i	tire slip ratio	i = 1,..,4
ω_{w_i}	tire angular speed,	
ζ_i	tire velocity angle	
ν_i	tire slip angle	$(= \delta_i - \zeta_i)$

With tire pressure, tire camber angle, and road and tire physical parameters fixed, the forces generated at the tire are functions of the slip ratio (A), slip angle (v), and the tire normal force (F_p). The set of curves in Figure 2.3 represent fits based on the tests of the Yokahama tires under laboratory conditions. The corresponding equations are given in Appendix B.

It should be noted that deviations from ideal, in terms of tire pressure and age, pavement material and weather conditions, will be reflected in the shape of the force-slip

experimentation. However, in the absence of experimental data, a simple multiplicative effect on the ideal curves is assumed (Bakker et. al., 1987). This is consistent with the theory that tire forces are proportional to the friction coefficients between tire and road surfaces. Typically, for average freeway operation, a factor of $\mu = 0.8$ is introduced. For wet road conditions, the factor is $\mu = 0.6$. For icy conditions, $\mu = 0.2$.

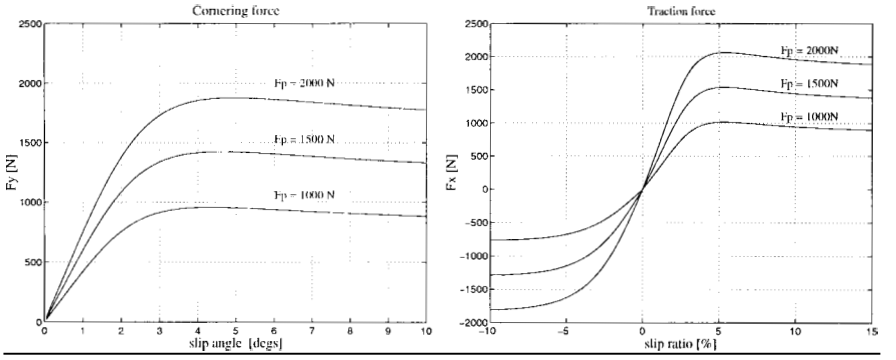

Figure 2.3: Force-slip characteristics of the Yokohama tire (Peng, 1992). μ=1.0 *(ideal road condition)*

The slip angle is found as the difference between the tire's orientation vector and its velocity vector (or $\nu_i = \delta_i - \zeta_i$). This velocity vector angle is found from the relationship

$$\zeta_{1,2} = tan^{-1}\frac{V_y + l_f\dot{\psi}}{V_x \mp \frac{s_f}{2}\dot{\psi}}, \qquad \zeta_{3,4} = tan^{-1}\frac{V_y - l_r\dot{\psi}}{V_x \mp \frac{s_r}{2}\dot{\psi}} \tag{2.21}$$

The slip ratio is computed as

$$\textit{traction} \qquad \lambda = \frac{r_w\omega_w - V_x}{r_w\omega_w} \geq 0 \tag{2.22}$$

$$\textit{braking} \qquad \lambda = \frac{r_w\omega_w - V_x}{V_x} < 0$$

Note: During normal highway cruising or mild acceleration on dry pavement, the slip is relatively small -- usually on the order of 1–2%. Consequently, many authors feel justified in invoking the no-slip assumption, *i.e.* $V_x = r_w\omega_w$, to eliminate the wheel states.

However, this assumption breaks down for large slips (such as occurs under adverse weather conditions or during emergency maneuvers).

A combined maneuver modification:

It is stressed that the preceding curves were obtained from *traction-only* and *cornering-only* tests and do not assume any longitudinal and lateral force coupling. Yet, the amount of traction available from the tire patch is necessarily limited, and hence, there must exist some relationship between the lateral and longitudinal forces. This relationship is popularly expressed in the idea of a friction ellipse (Fig 2.4) (Gillespie, 1992).

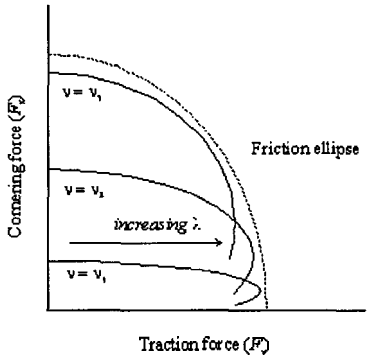

Figure 2.4: The friction ellipse construct representing the interdependence of traction and cornering forces on slip ratio (λ) and slip angle (ν): $\nu_3 > \nu_2 > \nu_1$.

Consistent with the friction ellipse hypothesis, Bakker (1989) proposed a squared-norm correction factor for combined maneuvers

$$\sigma = \sqrt{\left(\frac{\lambda}{\lambda_m}\right)^2 + \left(\frac{\nu}{\nu_m}\right)^2} \tag{2.23}$$

where the terms, λ_m and ν_m, refer to the slip values where the respective forces are maximum. Let $F_y(\nu)$ denote the dependence of the cornering force on the slip angle. Similarly, let $F_x(\lambda)$ denote the dependence of the traction force on the slip ratio. In addition, define as the modified slip quantities: $\lambda^* = \lambda_m \sigma$; $\nu^* = \nu_m \sigma$.

Then, the combined forces are modified according to

$$F_x = \frac{\lambda}{\lambda^*} F_x(\lambda^*) \qquad F_y = \frac{\nu}{\nu^*} F_y(\nu^*) \tag{2.24}$$

2.2.4 Transmission and drive train submodel

The transmission and drive-train serve as the link between the power generation mechanisms (engine and brakes) and the external dissipation mechanisms (traction and cornering forces). It receives as inputs, the net engine and brake torques, and outputs the necessary wheel slips to generate the traction forces required to propel the vehicle. There are four independent states associated with the drive train: the wheel angular velocities. Conversely, there are no independent states associated with the transmission since we model only a steady-state mapping between the engine and drive train.

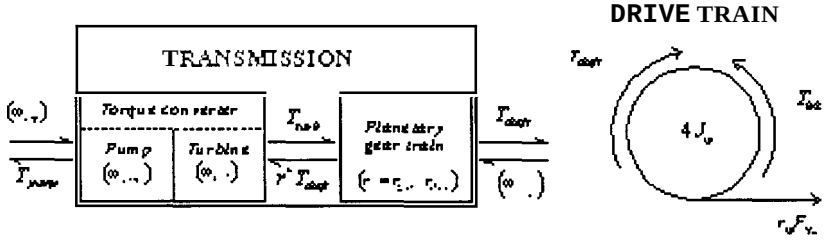

Figure 2.5: Schematic of transmission and drive-train submodel.

Variables introduced in this subsection are summarized below:

ω_{pump}	pump speed
ω_{turb}	turbine speed
ω_{w_i}	angular speed of i^{th} wheel, $i = 1, ..,4$
J_W	wheel polar moment
T_{pump}	pump torque
T_{turb}	turbine torque
T_{brk}	brake torque
T_{shaft}	drive shaft torque
r_{gear}	transmission gear ratio
r_{drive}	drive ratio

Drive train:

For a front wheel drive vehicle, the torque balance about each wheel yields

$$J_{w_i}\dot{\omega}_{w_i} = \frac{1}{2}T_{shaft} - \frac{3}{10}T_{brake} - r_{w_i}F_{x_i} \qquad \text{i = 1,2 (front)} \tag{2.25}$$

$$J_{w_i}\dot{\omega}_{w_i} = -\frac{2}{10}T_{brk} - r_{w_i}F_{x_i} \qquad i = 3,4 \text{ (rear)}$$

where T_{brk} is the total available braking torque, and T_{shaft} is the drive-shaft torque. The even distribution of the shaft torque reflects the action of the drive differential, while the front/back distribution of the brake torque follows the general "rule of thumb" split of 60%/40% for disc-drum brakes.

Transmission:

The shaft torque is obtained from the output of the transmission, which consists of a planetary gear set connected with a torque converter (Fig 2.6). Neglecting drive shaft torsion and gear shift dynamics, the torques **and** speeds across the planetary gear set are

$$T_{shaft} = \frac{1}{r_{gear}r_{drive}}T_{turb} \tag{2.26}$$

$$\omega_{turb} = \frac{1}{r_{gear}r_{drive}}\omega_{w_{ave}}$$

where $\omega_{w_{ave}}$ is the average speed of the front two wheels, and T_{turb} is the output of the torque converter. This torque converter is a bi-modal (*fluid*, ***mechanical)*** coupling between the engine and drive shafts, and acts primarily to smooth speed transmission during a gear shifts.

During periods of high torque transfer, the coupling is *fluidic*. Since the dynamics of the fluid are relatively fast, we can neglect torque production delays and time constants. This being the case, the input and output of the torque converter can be obtained from steady-state maps indexed by the speed ratio across the torque converter (Hedrick et. al., 1991)

$$T_{pump} = f_{in}(\frac{\omega_{turb}}{\omega_{pump}}, \omega_{pump}) \qquad input \tag{2.27}$$

$$T_{turb} = f_{out}(\frac{\omega_{turb}}{\omega_{pump}}, \omega_{pump}) \qquad output$$

where ω_{turb} is the turbine (output) speed and ω_{pump} is the pump (input) speed.

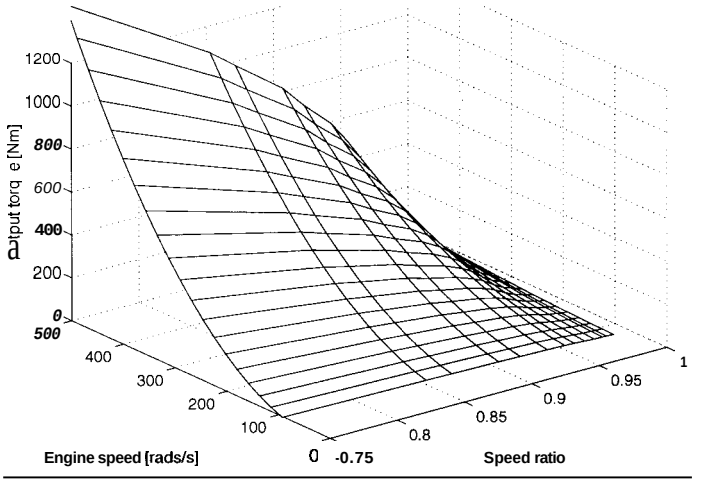

Figure 2.6: Typical turbine torque as a function of pump speed and speed ratio across the torque converter.

During steady-state cruising operation, the torque converter acts in the ***locked*** mode. In the locked position, the speeds and torques across the converter are matched *i.e.* $T_{pump} = T_{turb}$ and $\omega_{pump} = \omega_{turb}$.

2.2.5 Engine submodel

There has been a large body of work devoted to the development of engine models, ranging from discrete cylinder event models to continuous torque generation models (Choi, 1994). Nevertheless, for the purpose of longitudinal control, it has been shown that the continuous four-stroke spark ignition Moskwa-Hedrick (1987) model is adequate (McMahon et. al., 1993). We utilize a simplified two-state version of this

model, with the engine speed (ω_{eng}) and manifold air mass (m_a) as the state variables, the throttle (α) as the input, and the net engine torque (T_{net}) as the output (Fig 2.7).

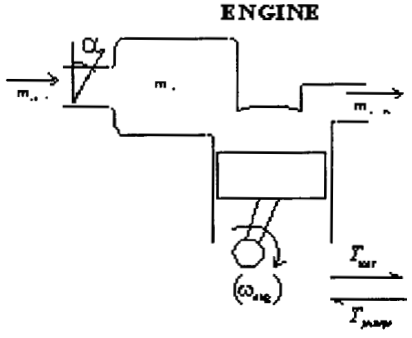

Figure 2.7: Schematic of **engine submodel.**

Variables in this subsection are:

α	throttle angle
ω_{eng}	engine speed
m_a	mass of air in manifold
$\dot{m}_{a\,in}$	rate of airflow into manifold
$\dot{m}_{a\,out}$	rate of airflow out of manifold
J_{eng}	engine polar moment of inertia
T_{pump}	engine load from torque converter pump
T_{net}	net engine output torque

The engine speed is governed by

$$J_{eng}\dot{\omega}_{eng} = T_{net} - T_{pump} \tag{2.28}$$

In the Moskwa-Hedrick model, T_{net} is the difference between the steady-state indicated (or combustion) engine torque, Ti, and the friction torque, Tf. The indicated engine torque was modeled as a continuous function

$$T_i = f_{ind}\left(\dot{m}_{a\,out}(\Delta t_{it}),\ \omega_{eng}(\Delta t_{it}),\ \Delta t_{st},\ \Delta t_{it}\right) \tag{2.29}$$

where Δt_{st} is the spark-to-torque production delay, and Δt_{it} is the intake-to-torque production delay. The two time delays are characteristic of the cyclic nature of the engine, and hence, varies inversely with engine speed. Similarly, the friction torque was found from

$$T_f = f_{frict}\left(\dot{m}_{a\,out},\ \omega_{eng}\right) \tag{2.30}$$

However, computer simulations have shown that under typical highway operations, *i.e.* high engine speeds, the two time delays can be largely ignored. Consequently, eqs (2.29-30) can be discarded in favor of a single steady-state mapping (Fig 2.8) of the two engine states

$$T_{net} = f_{net}\left(m_a,\ \omega_{eng}\right) \tag{2.31}$$

where the $\dot{m}_{a\,out}$ in (2.29-30) has been replaced by m_a. This arises from the fact that, without the engine delay and under ideal gas behavior (McMahon, et. al., 1992)

$$\dot{m}_{a\,out} = f_m\left(m_a,\ \omega_{eng}\right)$$

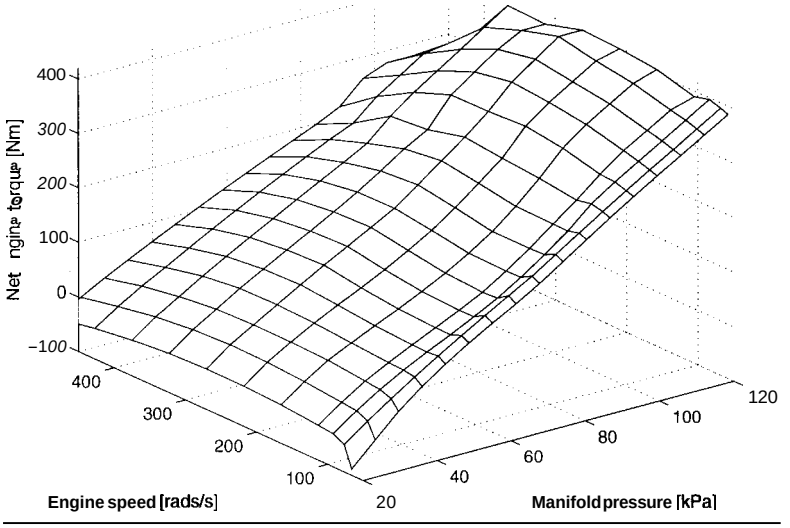

Figure 2.8: Torque production map of Ford V-8 5.0L engine.

The second engine state variable is governed by the continuity flow equation

$$\dot{m}_a = \dot{m}_{a\,in} - \dot{m}_{a\,out} \tag{2.32}$$

where $\dot{m}_{a\,in}$ is the air flow into the manifold, which is influenced by the throttle input, α, according to

$$\dot{m}_{a\,in} = MAX \cdot PRI(m_a) \cdot TC(\alpha) \tag{2.33}$$

MAX is an engine-specific constant indicating the maximum intake airflow; $PRI(\cdot)$ is called the manifold pressure influence function; and $TC(\cdot)$ is the throttle characteristic function (McMahon and Hedrick, 1989).

2.2.6 Brakes submodel

Early brake models adapted for use in longitudinal control studies were usually approximate models which consisted of a pure time delay and first-order linear dynamics (McMahon et. al., 1990). However, Gerdes et. al. (1994) showed that this model is inadequate for the control demands associated with an IVHS application, where low torques but quick response times are required. Indeed, due to the presence of "hard" nonlinearities, such as deadzones and hysteresis, any linear description of the brake dynamics falls short.

The brake submodel considered here (Hedrick et. al., 1995) consists of the dynamics of the master cylinder, vacuum booster, and the brake lines (Fig 2.9). The brakes are actuated by the push-rod, F_{pr}, and outputs the total torque available to the wheels, T_{brk}. Its states are T_{brk} and the mass of air in the apply and vacuum chambers, m_{aa} and m_{av}, respectively.

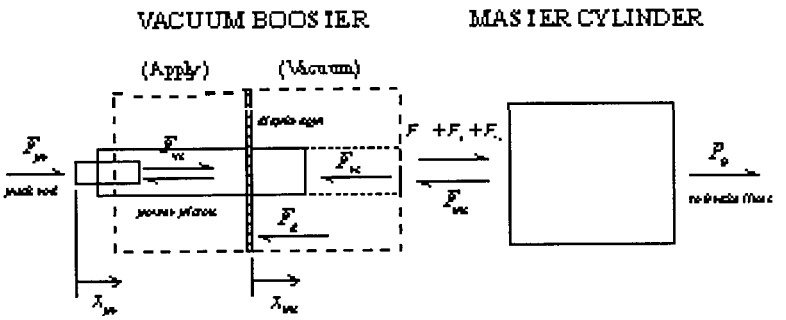

Figure 2.9: Schematic of **brake submodel.**

Variables and parameters in this subsection are:

A_d	diaphragm area
A_{mc}	master cylinder booster area
F_d	diaphragm force
F_{mc}	master cylinder force
F_{pr}	push rod force
F_{ps}	master cylinder preload
F_{rs0}	return spring preload
F_{vs0}	valve spring preload
$P_{a\,(v)}$	pressure in apply (vacuum) chamber
P_0	initial equilibrium pressure in both booster chambers
r	ratio of pushrod area to total master cylinder contact area
$V_{a0\,(v0)}$	initial apply (vacuum) chamber volume
x_{mc}	master cylinder (or alternatively, diaphragm wall) displacement
x_{pr}	push rod displacement

Vacuum booster:

The vacuum booster consists of 2 compartments, the apply and vacuum chambers, separated by a moving diaphragm, and acts primarily to provide constant amplification of the force applied by the driver (or in our case, the actuator) over the entire length of brake pedal travel. This booster is actuated by the motion of the pushrod, which contacts the master cylinder and some valve springs connected to the power piston.

Neglecting all the inertia effects, a force balance about the push rod yields

$$F_{pr} - F_{vs} - rF_{mc} = 0 \qquad \textbf{(2.34)}$$

where the nonlinear valve spring force is governed by the relative motion of the push rod and power piston

$$F_{vs} = F_{vs0} + K_{vs}(x)\left\{x_{pr} - x_{mc}\right\} \tag{2.35}$$

and F_{mc} is the master cylinder reaction force. The notation $K(x)$ is meant to indicate the spring stiffness' dependence on deflection.

The effect of the relative push rod motion on the thermodynamics of the vacuum booster can be divided into three distinct regimes, which give rise to the deadzone and hysteresis behavior observed in brake systems

$$\begin{aligned} 0 \le \left(x_{pr} - x_{mc}\right) < x_h \qquad & \textbf{\textit{release}} \\ x_h \le \left(x_{pr} - x_{mc}\right) < x_a \qquad & \textbf{\textit{hold}} \\ x_a \le \left(x_{pr} - x_{mc}\right) < x_s \qquad & \textit{apply} \end{aligned} \tag{2.36}$$

In each of the three regions, the chamber state variables are governed by

$$\dot{m}_{aa} = \begin{cases} c_{av}\left\{P_v - P_a\right\} \\ 0 \\ c_{aa}\left\{P_{atm} - P_{pa}\right\} \end{cases} \tag{2.37}$$

$$\dot{m}_{av} = \begin{cases} c_{vm}\left\{\left\{P_m + P_0\right\} - P_v\right\} + c_{av}\left\{P_a - P_v\right\} \\ c_{vm}\left\{\left\{P_m + P_0\right\} - P_v\right\} \\ c_{vm}\left\{\left\{P_m + P_0\right\} - P_v\right\} \end{cases} \tag{2.38}$$

where the pressures are given by the ideal gas law

$$P_a = \frac{m_{aa} RT}{V_{a0} + A_d x_{mc}} \tag{2.39}$$

$$P_v = \frac{m_{av} RT}{V_{v0} - A_d x_{mc}} \tag{2.40}$$

A similar force balance about the power piston yields

$$F_{vs} + F_d - F_{rs} - \{1 - r\} F_{mc} = 0 \tag{2.41}$$

with the diaphragm force being given by

$$F_d = \left\{P_a - P_v\right\} A_d \tag{2.42}$$

and the return spring force given by

$$F_{rs} = F_{rs0} + K_{rs} x_{mc} \tag{2.43}$$

Master cylinder:

The master cylinder piston is forced to move by the booster power piston. This motion, after some initial travel, displaces fluid from the master cylinder and into the brake lines, giving rise to the brake pressure

$$P_b = \frac{F_{mc}}{A_{mc}} \tag{2.44}$$

where the force applied to the master cylinder is given by

$$F_{mc} = K_{mx}(x)\left\{x_{mc} - x_{cp}\right\} + F_{ps} \tag{2.45}$$

The x_{cp} is the motion of the master cylinder piston measured after the "some initial travel" required by the piston to seal the fluid reservoir off from backflow. This phenomenon is the second source of deadzone behavior in the brakes.

Brake lines, valves and brakes:

The brake fluid, after leaving the master cylinder is affected by such diverse variables as friction, temperature, velocity, travel length, and valve characteristics. Efforts to model this behavior have not been definitive and do not yield any compact description of dynamics. For these reasons, Gerdes et. al. (1994) resorted to a dynamic mapping between the fluid pressure measured at the master cylinder and the brake torques

$$T_{brk} = \frac{1}{\tau_{brk}}\left\{f_b(P_b)P_b - T_{brk}\right\} \tag{2.46}$$

where $f_b(\cdot)$ gives a measure of the losses associated with fluid travel through the brake lines and τ_{brk} is the propagation delay.

2.2.7 Actuators

The vehicle's three actuators are all modeled as linear, first-order elements, with the following time constants

$\tau_{pr} = 0.075\ ms$ brake actuator

$\tau_{\delta} = 0.125\ ms$ steering actuator

$\tau_{\alpha} = 0.050\ ms$ throttle actuator

2.3 Control model

The simulation model, while adequately describing the true dynamic response of the vehicle, is nevertheless too complex for analysis and model-based controller design. Hence, it is necessary to make simplifying assumptions that will reduce the model to a tractable form, yet still capture fundamental plant behavior. The basis for each simplifying assumption are drawn from computer simulations, *ad hoc* comparisons of relative magnitudes, or historical results based on singular perturbation or linearization techniques.

Specifically, the main assumptions utilized in the simplified model are:

i) no gradient or superelevation effects

ii) negligible roll, pitch, and vertical motions

iii) sufficiently fast brake dynamics

iv) sufficiently fast manifold dynamics

v) locked torque converter

vi) dynamics of left and right sides are identical (bicycle model)

vii) negligible slip between tire and pavement

(i) We assume a flat terrain in order to lessen the mathematical complexity. Although, the results can be easily extended to include gradient or superelevation effects.

(ii) Computer simulations reveal that within the normal range of freeway maneuvers on flat roads, the roll, pitch and vertical motions can be discarded without appreciably effecting the longitudinal and lateral dynamics.

(iii) As discussed in the brake modeling section, the open-loop brake dynamics are generally appreciable. However, since the focus of this study is not on the actual mechanisms of brake torque control, we can assume the existence of an inner control loop which yields relatively fast closed-loop poles (Maciuca and Hedrick, 1994). Thus, for all intents and purposes, the overall brake dynamics can be discounted.

(iv) The locked torque converter assumption derives from the fact that, for most passenger vehicles, the torque converter is mechanically locked during 4^{th} gear operation. Nevertheless, even without the physical lock at the lower gears, the relative slip between the turbine and pump is less than 10% for most torque demands (recall Fig. 2.6).

(v) McMahon (1994) showed that in 4^{th} gear operation (with a locked torque converter), the eigenvalue associated with the manifold dynamics is generally at least 40 times faster than the eigenvalue associated with the engine speed. In lower gear operations, we can similarly assume (as in the brakes system) the existence of a sufficiently fast inner control loop.

(vi) The bicycle assumption (Fig 2.10) is commonly accepted in lateral control studies and agrees well with experimental and simulation (of the full model) results.

(vii) During dry road operations, the no-slip assumption is reasonable for cruising, accelerations, and moderate braking maneuvers (where the actual slip is usually below 4%). Departures from this condition occur with heavy braking, or during operations in

wet or icy road conditions. Consequently, this limitation should be kept in mind when considering the range of model effectiveness.

Under assumptions (i)-(iv), the model can be reduced to the following eight state equations

$$m\left[\dot{V}_x - V_y\dot{\psi}\right] = \sum_{i=1}^{4} F_{A_i} - C_x V_x^2 - F_{roll} \tag{2.47}$$

$$m\left[\dot{V}_y + V_x\dot{\psi}\right] = \sum_{i=1}^{4} F_{B_i} - C_y V_y^2$$

$$I_z\ddot{\psi} = M_z$$

$$J_{w_i}\dot{\omega}_{w_i} = \frac{1}{2}T_{shaft} - \frac{3}{10}T_{brk} - r_{w_i}F_{x_i} \qquad i = 1,\ 2\ \ (\textit{front})$$

$$J_{w_i}\dot{\omega}_{w_i} = -\frac{1}{5}T_{brk} - r_{w_i}F_{x_i} \qquad i = 3,\ 4\ \ (\textit{rear})$$

$$J_{eng}\dot{\omega}_{eng} = T_{net} - T_{pump}$$

where the forces are given as before (2.13), the moment is found from

$$M_z = l_f\left\{F_{B_1} + F_{B_2}\right\} - l_r\left\{F_{B_3} + F_{B_4}\right\} - \frac{s_f}{2}\left\{F_{A_1} - F_{A_2}\right\} - \frac{s_r}{2}F_{A_3} - F_{A_4} \tag{2.48}$$

and the net engine torque, $T_{net} = f\left(m_a,\ \omega_{eng}\right)$, is found from (2.31). Note that in eliminating the brake submodel and manifold states, the vehicle inputs (longitudinal) becomes T_{net} and T_{brk}, instead of a and F_{pr}. These equations provide the point of departure for the following model derivations.

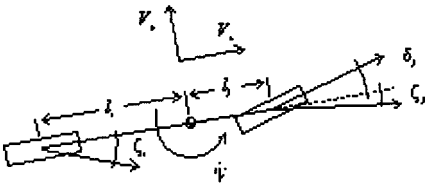

Figure 2.10: Kinematics bicycle model.

2.3.1 Simplified vehicle model I (SVM I)

The locked torque-converter and bicycle assumptions allows the engine speed state and the independent front wheel states to be collapsed into one state, *i.e.* $\dot{\omega}_{eng} = \dot{\omega}_{w_f}$. Thence, defining an effective gear ratio,

$$r_* \equiv r_{gear} \cdot r_{drive}$$

and recognizing that $C_s,\ K_T >> 1$, the state equations can be massaged into the form

$$\dot{V}_x = -\frac{1}{m} f_1 + \frac{2}{m}\left[\frac{\lambda_f F_{x_f}\left(\lambda_f^*\right)}{\lambda_f^*} + \frac{\lambda_r F_{x_r}\left(\lambda_r^*\right)}{\lambda_r^*} + \delta_f \frac{r_m \nu_f F_{y_f}\left(\nu_f^*\right)}{\nu_f^*}\right] \qquad \textit{(2.49)}$$

$$V_y = -\frac{1}{m} f_2 + \frac{2}{m}\frac{r_m \nu_f F_{y_f}\left(\nu_f^*\right)}{\nu_f^*}$$

$$\ddot{\psi} = -\frac{2}{I_z} l_r f_3 + \frac{2}{I_z} l_f \frac{r_m \nu_f F_{y_f}\left(\nu_f^*\right)}{\nu_f^*}$$

$$\dot{\omega}_{w_f} = -\frac{1}{J_{eng} + 2J_w r^{*2}}\left[2 r_w r^{*2} \frac{\lambda_f F_{x_f}\left(\lambda_f^*\right)}{\lambda_f^*}\right] + \frac{1}{J_{eng} + 2J_w r^{*2}}\left[r^* T_{net} - \frac{3}{5} r^{*2} T_{brk}\right]$$

$$\dot{\omega}_{w_r} = -\frac{1}{J_w} r_w \frac{\lambda_r F_{x_r}\left(\lambda_r^*\right)}{\lambda_r^*} - \frac{1}{J_w}\frac{1}{5} T_{brk}$$

where,

$$f_1 \equiv C_x V_x^2 + F_{roll} - m V_y \dot{\psi} \qquad \textit{(2.50)}$$

$$f_2 \equiv C_x V_y^2 + m V_x \dot{\psi} - 2\frac{r_m \nu_r F_{y_r}\left(\nu_r^*\right)}{\nu_r^*}$$

$$f_3 \equiv \frac{r_m \nu_r F_{y_r}\left(\nu_r^*\right)}{\nu_r^*}$$

This model shall be used to illustrate the lateral and longitudinal coupling in the subsequent chapter. Following is the derivation for the ***control*** model.

2.3.2 Simplified vehicle model II (SVM 11)

In contrast to **SVM I,** the model considered here is predicated upon the additional assumption that the tractive forces are unsaturated. The primary reason being that once into the nonlinear regime (or onto the edge of the friction ellipse), the tire patch becomes saturated and increased inputs can only lead to a loss of the total available tractive forces. Hence, in order to enhance the safety and robustness of the AHS, maneuvers that demand performance near the edge of the linear range should be scrupulously avoided.

It may be argued this performance limitation is too restrictive in a general sense because the available tractive forces impinge upon a number of other factors, such as tire and road conditions. In rebuttal to this point, we stress that under **no** circumstance should automated vehicle operations occur in unsafe environments. If the road conditions are inclement, the roadside planner should reduce vehicle speed in order to adhere to the linear region. The responsibility of maintaining the quality of the tires falls upon the individual vehicle owners, and should be rigorously regulated in the same manner as other required equipment, such as radar and radio.

We examine the possibility of a simpler expression for the cornering force. In many previous lateral control studies, a cornering stiffness term was introduced so as to make possible a simple, linear relationship between the steering input and the external forces. This cornering stiffness, C_S, is typically defined as

$$C_s \equiv \frac{\partial}{\partial \nu} F_y(\nu)\Big|_{\nu=0,\ h=O} \tag{2.51}$$

for a nominal value of F_p, calculated from a static moment balance. Then, for sufficiently small values of **v,** *i.e.* within the linear region of Figure 2.3, the cornering force can be approximated as

$$F_y \approx C_s \nu = C_s\{\delta - \zeta\} \tag{2.52}$$

However, in light of the combined maneuvering modifications introduced in (2.23-4), one may wonder whether the linearization given by (2.52) is valid in the presence of wheel slip. It is easy to see that as long as $\nu^* \le \nu_m$,

$$F_y \approx \frac{v}{v^*} C_s \nu^* = C_s \nu$$

and the cornering stiffness relation (2.52) still holds. Beyond the linear range, the cornering force is no longer proportional to ν^*, and it becomes difficult to separate the steering input in an affine fashion.

Finally, if the longitudinal wheel slip is also assumed to be negligible, the remaining two state variables for the wheels can also be eliminated, *i.e.* $r_w \dot{\omega}_{w_f} = r_w \dot{\omega}_{w_r} = V_x$. Define an effective vehicle inertia,

$$J^* \equiv m r_w^2 r^{*2} + J_{eng} + 4 J_w r^{*2}$$

Equation (2.49) can then be manipulated to yield the following expression

$$\dot{V}_x = -\frac{\left(r_w r^*\right)^2}{J^*} f_1 + \frac{\left(r_w r^*\right)^2}{J^*}\left[\frac{1}{r_w r^*}\left\{T_{net} - r^* T_{brk}\right\} + \delta_f C_{s_f}\left\{\delta_f - \zeta_f\right\}\right] \qquad (2.53)$$

$$\dot{V}_y = -\frac{1}{m} f_2 + \frac{2}{m} C_{s_f}\left\{\delta_f - \zeta_f\right\}$$

$$\ddot{\psi} = -\frac{2}{I_z} l_r f_3 + \frac{2}{I_z} l_f C_{s_f}\left\{\delta_f - \zeta_f\right\}$$

2.4 Conclusion

The **Complex** model includes engine, brakes, suspension, chassis, and drive-train submodels. The results indicate a satisfactory trade-off between fidelity and complexity under for all conceivable AHS operation regimes. Unfortunately, since we do not stress new modeling techniques, there is a dearth of experimental data for the model Pontiac

vehicle. This resulted in our relying, in some part, on adapted parameters from other vehicles. The effect of which is that the **Complex** model may not reflect the true open-loop vehicle response with great precision. However, as a simulation platform used to validate the performance of model-based controllers, this model is more than adequate since the *structure* of the plant is true. Our confidence is further buoyed by the fact that the vehicle submodels have been experimentally validated within the PATH Program.

Additionally, we have also proposed two control models of gradual complexities. These models were simplified from the **Complex** model and have been validated by comparing their input-output responses in a detailed simulation study. Some graphic results can be found in Tomizuka et al. (1995). The control models serve as the springboard from which to launch our controller discussion in the following chapter.

3 Controller design

3.1 Introduction

As has been remarked in the introduction, previous longitudinal and lateral control studies have progressed along independent tracks. Yet, from the kinematics results of the previous chapter, and from the conventional wisdom concerning tire force generation, it is evident that a coupling between the longitudinal and lateral dynamics exists, and may become significant under some maneuvers -- especially under adverse road conditions where large slip angles and slip ratios vie for limited available tire force. Narendran first considered the problem of dynamic coupling in the context of lane change maneuvers and demonstrated improved performance over the independent lateral and longitudinal controllers (1994). This chapter advances the combined study and examines the problem of lateral and longitudinal control in a more general setting.

The combined control problem is defined as the simultaneous regulation of the vehicle's relative longitudinal and lateral errors through the application of throttle, a, brakes, T_{brk}, and steering, δ. The longitudinal error, ε_i, is measured as the difference between the vehicle's longitudinal position (x_i) and the desired position ($x_{i-1} + L_0$). The lateral error, y_s, is distance taken as the perpendicular distance between the vehicle sensor and road center (Fig 3.1).

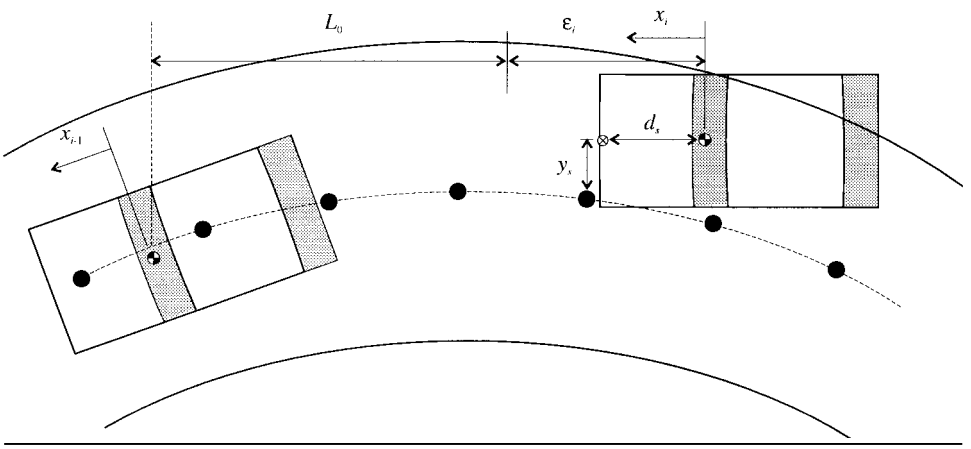

Figure 3.1: Combined lateral and longitudinal control objectives.

At first glance, the control problem is seen to be a rectangular 3-input, 2-output problem. However, since application of throttle and brakes can be designed for mutually exclusive operation, the two inputs can be collapsed into one, say the total *drive* torque at the wheels. Thus, for the sake of simplicity, T_{tot} and δ_f are considered as the inputs into a square 2-input, 2-output system. The problem of obtaining the desired controls, a and $T_{brk\,des}$, from T_{tot} is non-trivial and can be divided into three sub-problems: *i*) influencing the engine torque by controlling the manifold pressure (McMahon, 1994); *ii*) influencing the brake torque by controlling the brake pressure (Maciuca and Hedrick, 1994); and switching between the brakes and throttle (Gerdes, 1996).

With regards to the two-input, two-output problem, an obvious question that arises is that of quantifying the coupling between the longitudinal and lateral dynamics. If the dynamics were linear and affine with respect to the outputs, a simple measure would be to compare the relative magnitudes of the diagonal terms with the off-diagonal terms in the transfer function matrix. However, from a cursory examination of the simplified vehicle equations **(SVM I**,**II**), it is seen that the dynamics are neither linear nor affine.

Consequently, this leaves us with two recourses. One, should a coordinate transformation be sought that will yield a linear, affine representation? The drawback is that the new coordinates may not be physically meaningful. Or two, should computer simulations be utilized to obtain a quantitative description of the coupling for specific operating conditions? The drawback here is that this approach is *ad hoc* and may not yield a complete description. Thus, failing to find a single definitive answer, our choice, then, is: **both.**

Following this discussion, a robust Sliding Mode control law, based on the simplified model of **Chapter 2,** is derived. The combined control law is subsequently compared against independent lateral and longitudinal controllers in simulations. The basis of comparison draws from tracking performance and robustness against parameter errors and environmental disturbances.

3.2 Lateral and longitudinal coupling

3.2.1 Qualitative

For this analysis, only the case of front-wheel drive traction (*i.e.* $\lambda_f > 0,\ \lambda_r = 0$) is considered. This allows for a clear presentation of the argument without unnecessary algebraic clutter. Let the outputs be chosen as

$$y_1 = V_x \tag{3.2}$$

$$y_2 = V_y + V_x\left(\psi - \psi_{ref}\right)$$

where $\psi - \psi_{ref}$ is the heading angle deviation from some desired reference. **A** cursory examination of **SVM I** shows that the steering control is imbedded in the states. Consequently, in order to obtain an affine representation, the state space is dynamically extended to include the steering angle and slip ratio. The new steering control is chosen

as, $u_2 = 6_f$. Then, from the need to preserve the **vector relative degree,** the other control is chosen as, $u_1 = \lambda_f$.

The state vector is given by

$$\mathbf{x} = \begin{bmatrix} V_x & V_y & \dot{\psi} & \psi & \lambda_f & \delta_f \end{bmatrix}^T \in \Re^6 \tag{3.3}$$

Recalling our earlier commitment to remain within the linear region of the tire force curves **(chapter 2),** note that the plant can be described as $\mathbf{f}(\mathbf{x}) = \begin{bmatrix} ff_1 & ff_2 & ff_3 & ff_4 & 0 & 0 \end{bmatrix}$, where

$$ff_1 = -\frac{1}{m} f_1 + \frac{2}{m} K_{T_f} \lambda_f + \frac{2}{m} \delta_f C_{s_f} \left(\delta_f - \zeta_f \right) \tag{3.4}$$

$$ff_2 = -\frac{1}{m} f_2 + \frac{2}{m} C_{s_f} \left(\delta_f - \zeta_f \right)$$

$$ff_3 = -\frac{2l_r}{I_z} f_2 + \frac{2l_f}{I_z} C_{s_f} \left(\delta_f - \zeta_f \right)$$

$$ff_4 = \dot{\psi}$$

and K_{T_f} is the traction stiffness defined in a manner similar to C_{s_f} ,*i.e.*

$$K_{\tau} \equiv \frac{\partial}{ah} F_x(\lambda) \Big|_{v=0,\ h=O} \tag{3.5}$$

Then clearly, the system can be succinctly expressed as

$$\dot{x} = f(x) + g \cdot u \tag{3.6}$$

with $\mathbf{g} = \begin{bmatrix} 0 & 0 & 0 & 0 & 1 & 0 \\ 0 & 0 & 0 & 0 & 0 & 1 \end{bmatrix}^T$

It can be easily shown that (3.6), along with the output (3.2), has vector relative degree $\mathbf{r} = \begin{bmatrix} 2 & 2 \end{bmatrix}$. Indeed,

$$\ddot{\mathbf{y}} = \begin{bmatrix} L_{\mathbf{f}} L_{\mathbf{f}} y_1(\mathbf{x}) \\ L_{\mathbf{f}} L_{\mathbf{f}} y_2(\mathbf{x}) \end{bmatrix} + \begin{bmatrix} \dfrac{2K_{T_f}}{m} & \dfrac{2C_{s_f}\left(2\delta_f - \zeta_f\right)}{m} \\ \dfrac{2C_{sf}}{m} - \dfrac{2C_{s_f}\left(2\delta_f - \zeta_f\right)\tilde{\psi}}{m} & \dfrac{2K_{T_f}\tilde{\psi}}{m} \end{bmatrix} \begin{bmatrix} u_1 \\ u_2 \end{bmatrix} \tag{3.7}$$

$$= \mathbf{\Phi}\left(\mathbf{x}^*\right) + \mathbf{B}\left(\mathbf{x}^*\right)\mathbf{u}^*$$

where $\tilde{\psi}$ is the heading error.

In literature, $\mathbf{B}\left(\mathbf{x}^*\right) \in \Re^{2\times 2}$ is often known as the de-coupling matrix. **A** good measure of the coupling between u_1 and u_2 can be obtained by comparing the ratio of the off-diagonal terms of **B** to the diagonal terms, *i.e.*

$$\left|\frac{b_{12}}{b_{11}}\right| = \left|\frac{C_{s_f}\left(2\delta_f - \zeta_f\right)}{K_{T_f}}\right| \tag{3.8}$$

$$\left|\frac{b_{21}}{b_{22}}\right| = \left|\frac{K_{T_f}\tilde{\psi}}{C_{s_f} - C_{s_f}\left(2\delta_f - \zeta_f\right)\tilde{\psi}}\right|$$

From (3.8), it is seen that the dependence of y_1 on the second input channel grows as the steering angle becomes large. This agrees with our intuition; for certainly, we would expect the severity of the $y_1 - u_2$ coupling to increase as more cornering force is directed towards impeding the forward motion. Likewise, it is also observed that y_2 is increasingly dependent on the first input channel as the heading error increases. This should come as no surprise if one realizes that y_2 is merely the lateral rate of change of the vehicle *away* from the reference line. Thus, as the angle between the vehicle heading and this reference line increases, so should the component of longitudinal motion which contributes to $\ddot{y}_2$ also increase.

Still, we have offered but a general interpretation of (3.8). It is difficult to glean any more meaningful insights from (3.8) due to its being a nonlinear function of the states. However, if the states were to be constrained on the manifold, $\mathbf{f}(\mathbf{x}) = \mathbf{0}$, it is

possible to uniquely solve for $(V_x, V_y, \dot{\psi})$ for given values of (h_f, δ_f). Then, we can see how (3.8) evolve as (λ_f, δ_f) increases. The following set of plots are shown for $\tilde{\psi} = 4^\circ$ (Fig 3.2).

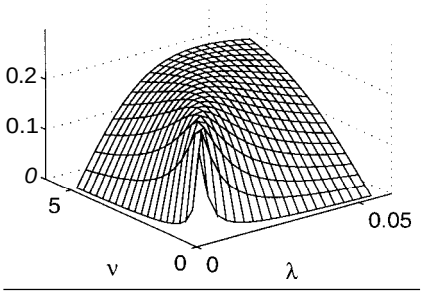

Figure 3.2a: $\left|\frac{b_{12}}{b_{11}}\right|$ as a function of **slip.**

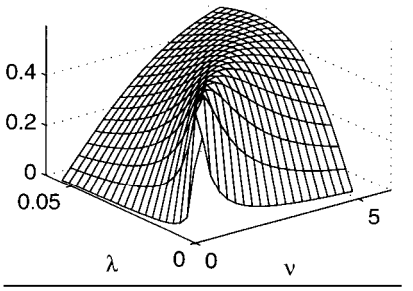

Figure 3.2b: $\left|\frac{b_{21}}{b_{22}}\right|$ as a function of slip.

As a final note, we concede that while the coupling is significant in some instances, it does not translate directly to a one-to-one correspondence to the coupling between the true vehicle inputs (throttle and steering) and the outputs (lateral and longitudinal errors). Nevertheless, it does yield a qualitative appreciation of the coupling present in the dynamics.

3.2.2 Quantitative

The vehicle input-output relation can be represented by the block diagram

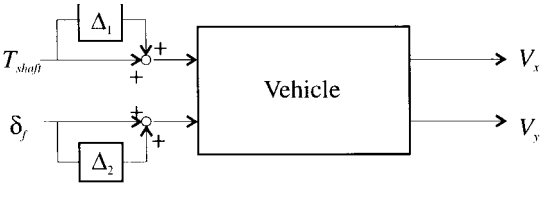

Figure 3.3: Block diagram of vehicle.

where the feed-forward gains, **A**, and Δ_2, represent perturbations at the inputs.

In order to illustrate the coupling between the longitudinal and lateral dynamics, the following simulations are conducted with the **Complex** model. The vehicle is given a set of nominal inputs (T_{shaft} = 215 Nm, δ_f = 1.72"). The corresponding longitudinal and lateral velocities are shown as solid lines (Figs 3.4a,b). The dashed lines represent the response of the vehicle due to non-zero input perturbations.

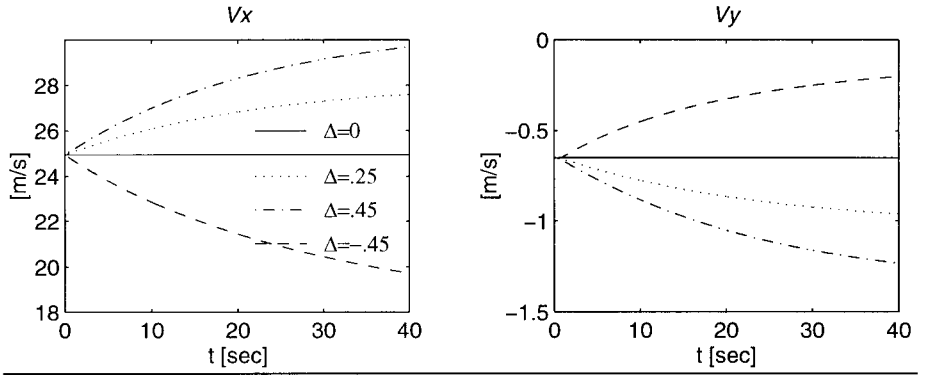

Figure 3.4a: Vehicle output as a function of shaft torque (Δ_1) perturbations; $\Delta_2 \equiv 0$.

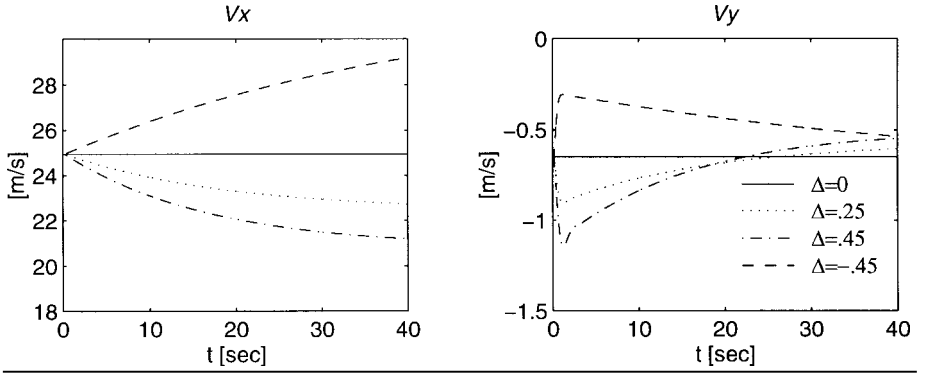

Figure 3.4b: Vehicle output as a function of steering (Δ_2) perturbations; $\Delta_1 \equiv 0$.

The plots in Figure 3.4 dispel some of the earlier conclusions drawn from Figure 3.3. In contrast to the previous section, it is seen here that the $y_2 - u_1$ coupling (*i.e.*

$|b_{21} / b_{\dot{\psi}}|$) is stronger than the y, $-u_2$ coupling (*i.e.* $|b_{12} / b_{11}|$). This comes back to the earlier statement in the introduction concerning the lack of direct correspondence between the true input-output relation and the transformed input-output relation. Consequently, the results from both section should be taken together with reservations. Nevertheless, we can conclude that a coupling between the longitudinal and lateral dynamics does exist and can be appreciable under certain operating conditions. This motivates our stated need for a combined control law which explicitly accounts for these cross-effects.

3.3 Lateral and longitudinal control design

Consider the system given by **SVM II**. As previously mentioned, an affine input-output representation may be obtained by augmenting the state space to include the vehicle controls, T_{tot} and δ_f. Then, the problem of finding the output-linearizing inputs become straightforward. Yet, the problem with this approach is that it involves differentiation of uncertainties associated with the plant. And since **SVM II** rely directly on tire parameters that are notoriously inaccurate, this method is clearly not feasible. Alternatively, Narendran (1994) showed that under certain rank conditions, the linearizing controls may be obtained for problems with separable inputs, *i.e.*

$$\dot{\mathbf{x}} = \mathbf{f}(\mathbf{x}) + \sum_1^m \mathbf{p}_j(\mathbf{x})\mathbf{l}_j(\mathbf{u}_j) \tag{3.9}$$

However, under the more general form of (3.7), a more general solution is not always possible.

Fortunately, there is a third alternative. That is, suppose an approximate, numerical linearizing control, $w(\mathbf{x})$, is obtained. Then, the questions that must be asked are: *i)* under what conditions can an approximate linearizing control be obtained, and *ii)* whether the stability of the controlled plant is jeopardized under $w(\mathbf{x})$. The answers to these questions are given in Pham (1996). It suffices to say that **SVM** II satisfies the

conditions for the existence of $w(\mathbf{x})$. Moreover, boundary layer tracking can be assured under $w(\mathbf{x})$.

3.3.3 Vehicle control

The vehicle **(SVM 11),** under traction and steering control, can be described by

$$\begin{aligned} V_x &= k_1 f_1 + b_{11} T_{tot} + b_{12} C_{s_f} \left(\delta_f - \zeta_f \right) \cdot \delta_f \\ \dot{V}_y &= k_2 f_2 + b_2 C_{s_f} \left(\delta_f - \zeta_f \right) \\ \dot{\psi} &= k_3 f_3 + b_3 C_{s_f} \left(\delta_f - \zeta_f \right) \end{aligned} \tag{3.30}$$

where $T_{tot} = T_{net} + r^* r_w T_{brk}$, and the constants, k_i's and b_i's are appropriately defined from (2.56) and (2.61).

The output dynamics are given by

$$\begin{aligned} \dot{\varepsilon} &= V_x - V_{lead} \\ \dot{y}_s &= V_y + V_x \tilde{\psi} + d_s \dot{\psi} \end{aligned} \tag{3.31}$$

where d_s is the distance from the vehicle center of mass to the vehicle-mounted sensor (recall Fig 3.1).

It can be shown that (3.30) has vector relative degree, $\mathbf{r} = [2 \quad 2]^T$, with respect to the outputs, y_s and ε, **away** from $V_x = 0$. **Note:** This should not be surprising since it is well known that we can control the vehicle's direction with a steering input only when the vehicle is in motion $(V_x \neq 0)$. The above vector relative degree implies that the right surface dynamics are

$$\begin{bmatrix} s_1 \\ s_2 \end{bmatrix} \equiv \begin{bmatrix} \dot{\varepsilon} + \lambda_{11} \varepsilon + \lambda_{12} \int \varepsilon dt \\ \dot{y}_s + \lambda_{21} y_s + \lambda_{22} \int y_s dt \end{bmatrix} = \begin{bmatrix} 0 \\ 0 \end{bmatrix} \tag{3.32}$$

where the λ_i's are positive constants chosen with an eye towards ride comfort and actuation bandwidth.

Then, a single differentiation of **s** yields

$$\begin{aligned}
\dot{s}_1 &= k_1 f_1 - \dot{V}_{lead} + \lambda_{11}\dot{\varepsilon} + \lambda_{12}\varepsilon + k_{11}T_{tot} + k_{12}C_{s_f}\left(\delta_f - \zeta_f\right)\delta_f \\
\dot{s}_2 &= k_1 f_1 \tilde{\psi} + k_2 f_2 + d_s\left(k_3 f_3\right) + V_x\dot{\tilde{\psi}} + \lambda_{21}\dot{y}_s + \lambda_{22}y_s \\
&\quad + \left(k_{11}T_{net} + k_{12}C_{s_f}\left(\delta_f - \zeta_f\right)\delta_f\right)\tilde{\psi} + \left(k_2 + d_s k_3\right)C_{s_f}\left(\delta_f - \zeta_f\right)
\end{aligned} \tag{3.33}$$

Choose the reaching control as

$$\mathbf{w} \equiv -\begin{bmatrix}\eta_1 s_1 & \eta_2 s_2\end{bmatrix}^T \tag{3.34}$$

This results in the necessity to solve the following homogenous equations for T_{net} and δ_f

$$\begin{aligned}
0 &= k_1 f_1 - \dot{V}_{lead} + \lambda_{11}\dot{\varepsilon} + \lambda_{12}\varepsilon + w_1 + k_{11}T_{tot} + k_{12}\delta_f C_{s_f}\left(\delta_f - \zeta_f\right) \\
0 &= k_1 f_1 \tilde{\psi} + k_2 f_2 + d_s\left(k_3 f_3\right) + V_x\dot{\tilde{\psi}} + \lambda_{21}\gamma_2 + \lambda_{22}y_s + w_2 \\
&\quad + \left(k_{11}T_{tot} + k_{12}\delta_f C_{s_f}\left(\delta_f - \zeta_f\right)\right)\tilde{\psi} + \left(k_2 + d_s k_3\right)C_{s_f}\left(\delta_f - \zeta_f\right)
\end{aligned} \tag{3.35}$$

Obviously, the range of the control space is limited by the power of the engine and the amount of available tire forces. Hence, the solvability of (3.35) depend on the value of the states and the errors.

In order to decrease the chance of control saturation (or equivalently, to strengthen the range condition), the linear attraction term can be replaced with a smooth, signum-like term

$$\mathbf{w}' \equiv -\begin{bmatrix}\dfrac{\eta_1 s_1}{\sqrt{s_1^2 + \gamma_1^2}} & \dfrac{\eta_2 s_2}{\sqrt{s_2^2 + \gamma_2^2}}\end{bmatrix}^T \tag{3.36}$$

where $0 < \gamma_i << \eta_i$. The use of this term, in lieu of (3.35), provides greater control in the region, $s_i < 1$, and relaxes the control effort for $s_i > 1$. Consequently, (3.36) ensures asymptotic convergence to a tighter boundary layer, while simultaneously limiting the attraction rate for large perturbations or initial conditions. In the following, it is assumed that the region of vehicle operation is reachable by the controls.

At any point, $\mathbf{x}_0$, in this reachable region, the problem reduces to solving

$$
\begin{aligned}
&b_{11}T_{tot} + b_{12}\delta_f C_{s_f}\left(\delta_f - \zeta_f\right) = tt_1\left(\mathbf{x}_0\right) \\
&\left(b_2 + d_s b_3\right)C_{s_f}\left(\delta_f - \zeta_f\right) = tt_2\left(\mathbf{x}_0\right)
\end{aligned}
\tag{3.37}
$$

for T_{net} and δ_f, where

$$
\begin{aligned}
tt_1 &= -\left\{k_1 f_1 - \dot{V}_{lead} + \lambda_{11}\dot{\varepsilon} + \lambda_{12}\varepsilon + w_1'\right\} \\
tt_2 &= -\left\{\left(k_1 f_1 + tt_1\right)\tilde{\psi} + k_2 f_2 + d_s\left(k_3 f_3\right) + V_x\dot{\tilde{\psi}} + \lambda_{21}\dot{y}_s + \lambda_{22}y_s + w_2'\right\}
\end{aligned}
\tag{3.38}
$$

The determinant of the Jacobean of the left-hand side of (3.41) is given by

$$
\begin{aligned}
\begin{vmatrix} b_{11} & b_{12}C_{s_f}\left(2\delta_f - \zeta_f\right) \\ 0 & C_{s_f}\left(b_2 + d_s b_3\right) \end{vmatrix} &= b_{11}C_{s_f}\left(b_2 + d_s b_3\right) \\
&\neq 0
\end{aligned}
\tag{3.39}
$$

Thus, a unique solution exists. **As** has been mentioned, the controls can be approximately obtained by any number of search methods. Fortunately, due to the upper triangular form of (3.38), there is no need to resort to such extreme measures. The exact solution may be obtained by first solving for δ_f in the *tt2* equation (3.37). Then, with this value of δ_f, solve for T_{net} in the tt_1 equation.

This results in the following expressions for the controls

$$
\begin{aligned}
\delta_f &= -\frac{\left\{\left(V_{lead} - \lambda_{11}\dot{\varepsilon} - \lambda_{12}\varepsilon - w_1'\right)\tilde{\psi} + k_2 f_2 + d_s\left(k_3 f_3\right) + V_x\dot{\tilde{\psi}} + \lambda_{21}\dot{y}_s + \lambda_{22}y_s + w_2'\right\}}{C_{s_f}\left(b_2 + d_s b_3\right)} + \zeta_f \\
T_{tot} &= -\frac{1}{b_{11}}\left\{k_1 f_1 - V_{lead} + \lambda_{11}\dot{\varepsilon} + \lambda_{12}\varepsilon + w_1' + b_{12}\left|\delta_f C_{s_f}\left(\delta_f - \zeta_f\right)\right|\right\}
\end{aligned}
\tag{3.40}
$$

Note: The problem of obtaining the desired throttle (a)or brake control (F_{pr}) from T_{tot} has been solved by McMahon (1994). The solution makes use of the multiple-sliding surface methodology to avoid direct differentiation of errors associated with the engine maps. In effect, T_{net} (obtained from the primary surface) acts as the desired "output" from which a desired manifold pressure (or brake torque) is obtained.

Then, problem defined by the secondary surface, *i.e.*

$$\begin{bmatrix} S_3 \\ S_4 \end{bmatrix} \equiv \begin{bmatrix} m_a - m_{a\,des} \\ T_{brk} - T_{brk\,des} \end{bmatrix} = \begin{bmatrix} 0 \\ 0 \end{bmatrix} \tag{3.41}$$

is to drive $m_a \rightarrow m_{a\,des}$ with the throttle control, and $T_{brk} \rightarrow T_{brk\,des}$ with brake control.

3.4 Simulations

The combined control law of (3.40) is compared against independent lateral and longitudinal controllers in the following simulations. The independent controllers are derived from a straightforward application of the Sliding Mode technique to the de-coupled vehicle model, *i.e.*

$$\begin{aligned} V_x &= k_1 f_1 + b_{12} T_{tot} \\ \dot{V}_y &= k_2 f_2 + b_2 C_{sf} \left(\delta_f - \zeta_f \right) \\ \ddot{\psi} &= k_3 f_3 + b_3 C_{sf} \left(\delta_f - \zeta_f \right) \end{aligned} \tag{3.42}$$

The resulting control laws are then given by

$$\begin{aligned} \hat{\delta}_f &= \frac{k_2 f_2 + d_s \left(k_3 f_3 - \ddot{\psi}_{rd} \right) + V_x \dot{\tilde{\psi}} + \lambda_{21} \dot{y}_s + \lambda_{22} y_s + w_2'}{C_{s_f} \left(b_2 + d_s b_3 \right)} + \zeta_f \\ \hat{T}_{tot} &= -\frac{1}{b_{11}} \left\{ k_1 f_1 - \dot{V}_{lead} + \lambda_{11} \dot{\varepsilon} + \lambda_{12} \varepsilon + w_1' \right\} \end{aligned} \tag{3.43}$$

The set of gains used in the following simulations are shown in Table 3.1, and the vehicle parameter values are given in Appendix A.

Table 3.1: Controller gains.

$\lambda_{11} = 1.0$	$\lambda_{12} = 0.25$	$\eta_1 = 0.10$	$\gamma_1 = 0.01$
$\lambda_{21} = 1.4$	$\lambda_{22} = 0.49$	$\eta_2 = 0.50$	$\gamma_2 = 0.05$
$\lambda_{31} = \text{NA}$	$\lambda_{32} = \text{NA}$	$\eta_3 = 40.0$	$\gamma_3 = \text{NA}$
$\lambda_{41} = \text{NA}$	$\lambda_{42} = \text{NA}$	$\eta_4 = 40.0$	$\gamma_4 = \text{NA}$

The simulations are conducted with the **Complex** model and is numerically integrated with a 4th-order Runge-Kutta routine at 500 μsec increments. The internal states $\left(V_x, V_y, \dot{\psi}\right)$ are assumed known, as are the disturbances $\left(\dot{V}_{lead}, \dot{\psi}_{des}\right)$. The controls are updated every 20 msec.

3.4.1 Effect of lateral acceleration on longitudinal tracking

In the first set of simulations, we consider the effects of increasing lateral control activity on the longitudinal tracking performance of the combined and independent controllers. The simulation profiles are shown in Fig 3.6 below.

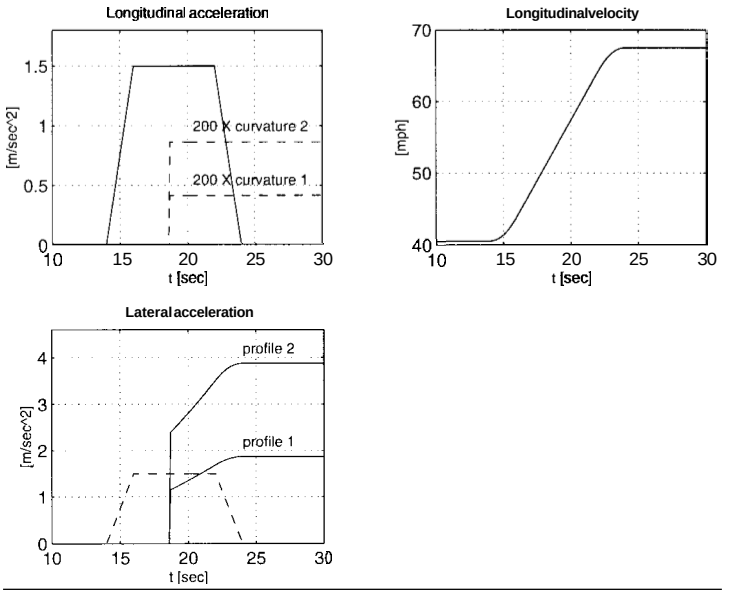

Figure 3.6: Commanded simulation profile. The longitudinal acceleration is held constant while road curvature is varied according to: $\rho_1 = 480\text{m}$; $\rho_2 = 197\text{m}$.

The first commanded profile represents a moderately demanding turn ($\rho = 480$ m), the likelihood of which is admittedly rare on typical highways. It is more likely to be

encountered on entrance/exit ramps and lane change maneuvers. On the other hand, the second profile (ρ = 197 m) represents a severely demanding maneuver which should not be expected in any context of **AHS** operation. Its use here represents the upper bound on the range of allowable maneuvers.

The longitudinal tracking errors resulting from the above two profiles are shown in Fig 3.7 for a road adhesion coefficient of $\mu = 0.8$. The value is assumed to be known to the controller. It is seen that there is negligible difference between the combined and independent controllers in the moderate maneuver case. The difference in the case of the second maneuver, however, is stark. Indeed, beyond the three-fold increase in performance, there is also a qualitative difference as the longitudinal error of the decoupled controller degrades to unacceptable levels in the steady-state.

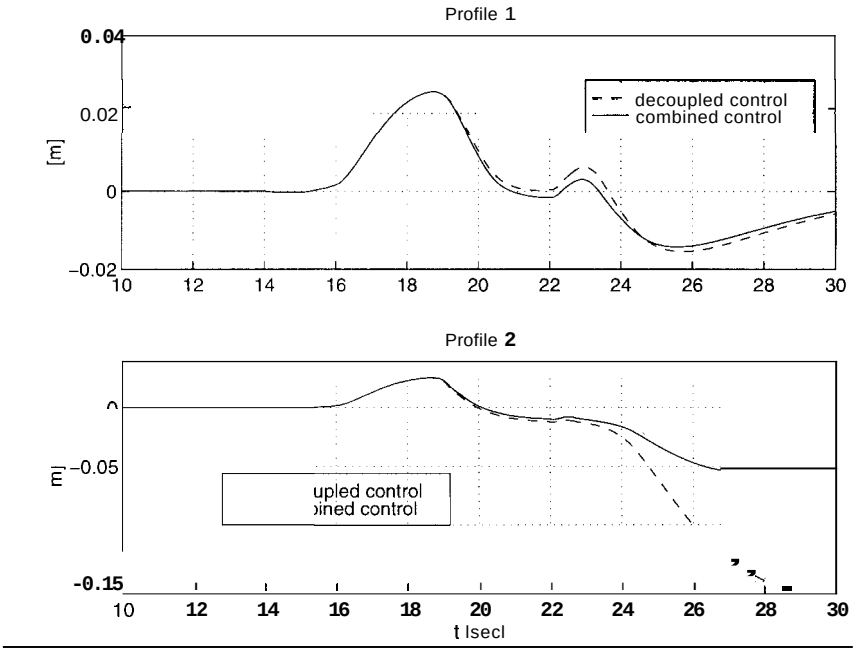

Figure 3.7: Longitudinal spacing error for maneuvers on dry road ($\mu = 0.8$).

The effect of decreased road adhesion is illustrated in Fig 3.8 for $\mu = 0.4$. Observe that error of the independent controller exhibits a lag relative to the error of the combined

controller. This indicates that the latter controller provides a larger phase margin, and hence, a greater margin of stability. The difference is more appreciable in this case of decreased of tire friction due to the fact that larger steering angles are required to generate the required lateral forces. This, in turn, results in larger coupling between the lateral and longitudinal dynamics (recall Fig 3.2).

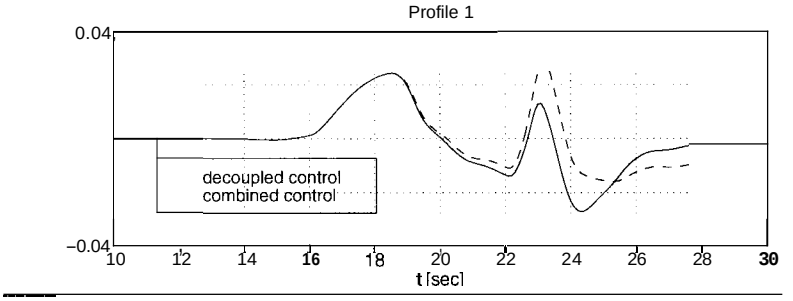

Figure 3.8: Longitudinal spacing error for maneuvers on wet road ($\mu = 0.4$).

3.4.2 Effect of longitudinal acceleration on lateral tracking

The effect of longitudinal demands on y_s is investigated in this section. The simulation conditions are depicted in Fig 3.9 below.

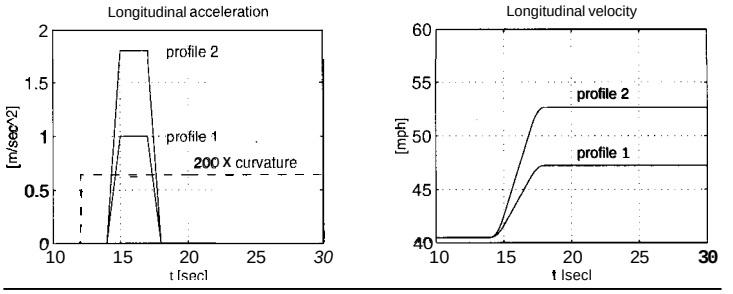

Figure 3.9: Commanded simulation profile. The curve is held fixed at $\rho = 279$m while lead vehicle acceleration is varied according to: $a_{lead} = 1.0$ m/s^2; $a_{lead} = 1.8$ m/s^2.

The associated lateral errors are shown in Fig 3.10. **As** before (in **section 3.5.1)** the performance gain afforded by the combined controller is minimal in the case of the

moderate acceleration profile. There is, however, a discernible phase difference between the errors of the two controllers. On the other hand, the performance of the combined controller is noticeably superior in terms of both error magnitude and phase in the case of the heavier acceleration (profile 2). Further, it should also be noted that, unlike the previous section, severe longitudinal accelerations are to be expected as matter of course.

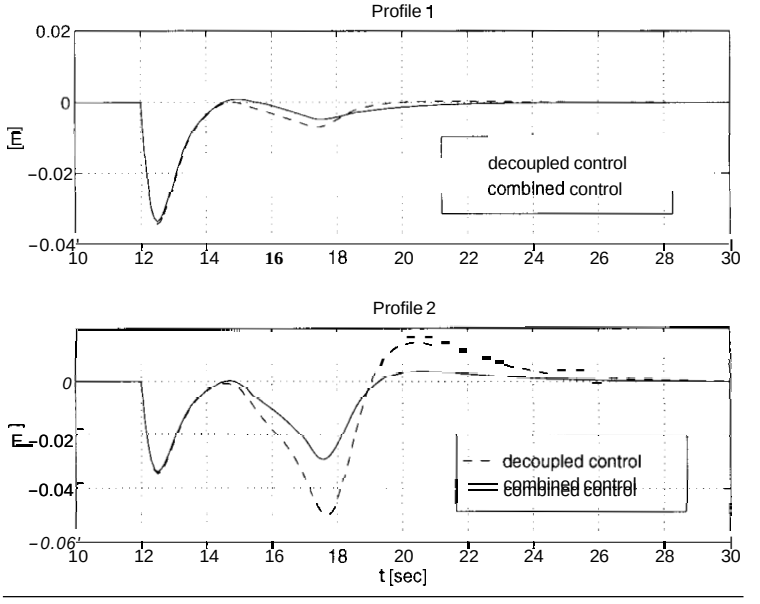

Figure 3.10: Lateral errors under combined maneuvers, $\dot{V}_x \geq 0$.

While the second profile in Fig 3.9 above represents the upper bound on accelerations attainable by the vehicle power plant, it is moderate in comparison to the values achievable by the braking system. Hence, it is expected that coupled control should be even more crucial during a combined braking/cornering maneuver. Following is a set of simulations conducted for a maximum deceleration of $\dot{V}_x = -4 \text{ m/s}^2$ (Fig 3.11-2).

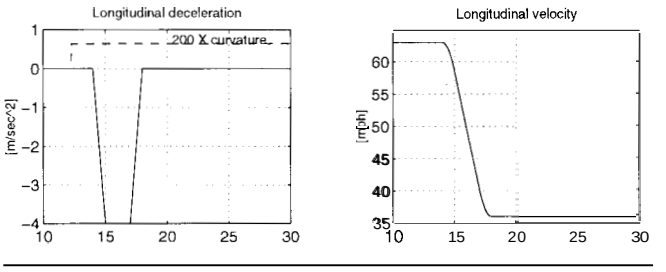

Figure 3.11: Commanded simulation profile. Combined braking/ cornering maneuver.

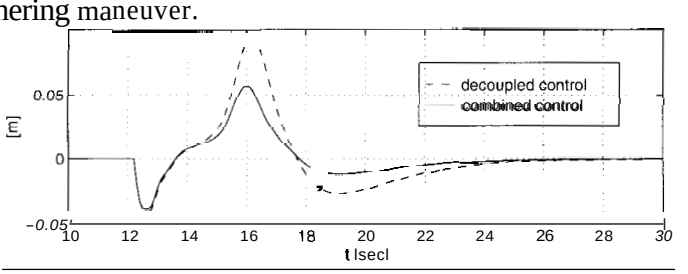

Figure 3.12: Lateral errors under combined maneuvers, $\dot{V}_x \leq 0$.

3.4.3 Robust performance

The robust demands of the AHS are especially demanding considering the wide range of operating conditions expected. We have already touched upon the uncertainties associated with tire and pavement conditions. Other significant parameter variations include the mass and the mass distribution. Additionally, there are also the effects of frontal and side wind gusts to consider.

It is well known that if the disturbances (or equivalently, the parameter errors) are bounded, the system trajectory may still be forced onto the sliding surface for sufficiently large reaching gain, η (3.36). Assuming an exact solution (3.18) in case of non-affine input, we conservatively require

$$\eta > \tilde{f}_{max} + \tilde{g}_{max} + d_{max} \tag{3.44}$$

where $\tilde{f}_{max}$ and $\tilde{g}_{max}$ are the maximum errors associated with the plant and input channel in the operating range of interest, and d_{max} is the maximum *unknown* disturbance.

Considering the range of uncertainties introduced in the following, it suffices to choose the gains as shown in Table 3.2 below.

Table 3.2: Robust controller gains.

$\lambda_{11} = 1.0$	$\lambda_{12} = 0.25$	$\eta_1 = \mathbf{0.20}$	$\gamma_1 = \mathbf{0.02}$
$\lambda_{21} = 1.4$	$\lambda_{22} = 0.49$	$\eta_2 = \mathbf{1.60}$	$\gamma_2 = \mathbf{0.16}$
$\lambda_{31} = \text{NA}$	$\lambda_{32} = \text{NA}$	$\eta_3 = 40.0$	$\gamma_3 = \text{NA}$
$\lambda_{41} = \text{NA}$	$\lambda_{42} = \text{NA}$	$\eta_4 = 40.0$	$\gamma_4 = \mathbf{NA}$

In order to provide some base-line for comparison, the controller with the signum-like attraction term (3.36) is compared with the linear attraction term, ηs, in the subsequent simulations. We call the former, **nonlinear,** and the latter, **linear.** The following simulations were conducted with profile 1 of Fig 3.9.

3.4.3a Cornering stiffness error

The effect of 100% cornering stiffness over-estimation error on lateral tracking performance is shown in Fig 3.13 below. The true road adhesion coefficient of $\mu = 0.4$ is estimated at $\hat{\mu} = 0.8$.

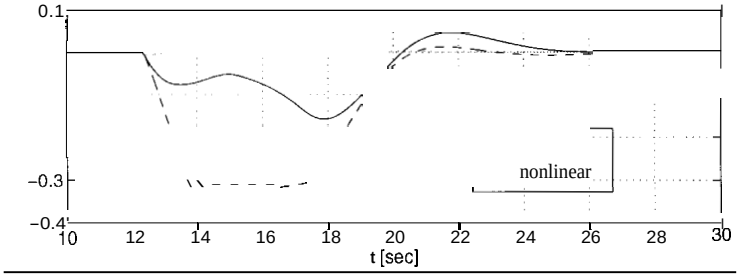

Figure 3.13: Lateral error, y_s, with +100% μ-estimation error ($\mu = 0.4$). The faint dotted line indicates nominal performance for the case of $\mu = 0.8$.

Observe that performance of the nonlinear attraction term is significantly better than that of the linear term. This results from the fact that the signum-like term affords

more control near the surface, $\mathbf{s} = \mathbf{0}$. The following simulation studies with different parameter error estimates demonstrate similar results.

3.4.3b Inertia error

Assuming a worst-case payload of 5 very large adults, the mass of the vehicle can be increased by as much as 700 kg. This also translates to an approximate increase in the yaw moment of inertia of 300 kg-m^2. Following are some plots showing the effect of under-estimates of vehicle inertia on longitudinal and lateral tracking (Fig 3.14). Note that some significant differences are observed between the linear and non-linear controllers.

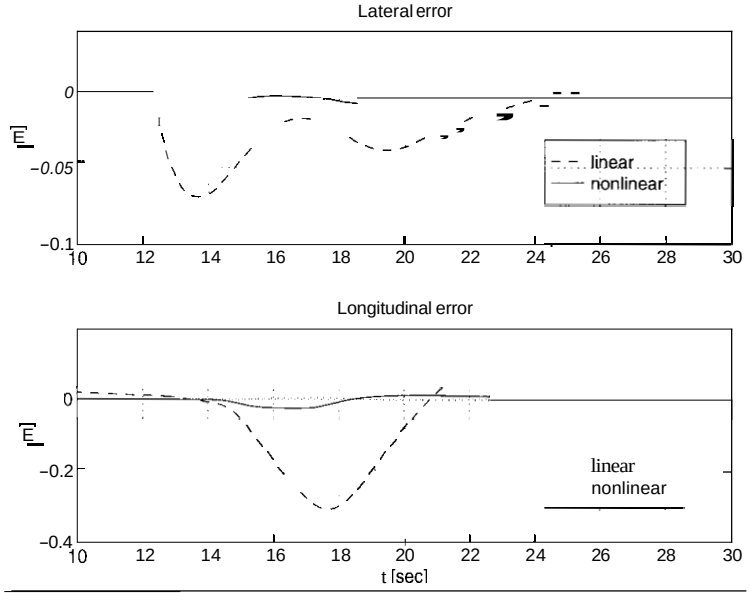

Figure 3.14: Lateral and longitudinal errors for inertia estimate errors.
$\hat{m} = 1573\,\text{kg}$, $\hat{I}_z = 2782\,\text{kg-m}^2$; $m = 2273\,\text{kg}$, $I_z = 3082\,\text{kg-m}^2$.
Faint dotted line indicates nominal performance, *i.e.* $\text{m} = \hat{m}$, $I_z = \hat{I}_z$.

3.4.3c Longitudinal wind gust

The effect of a 45 mph frontal wind gust is considered in Fig 3.15. The gust begins at $t = 14\,\text{sec}$, and endures for one second.

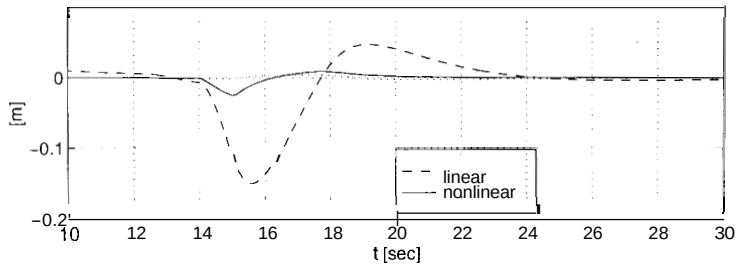

Figure 3.15: Longitudinal error with frontal wind gust of 20 m/s.

3.4.3d Lateral wind gust

Finally, we consider the effects of a 45 mph side wind gust on the lateral error. Again, the one second gust beings at $t = 14$ sec.

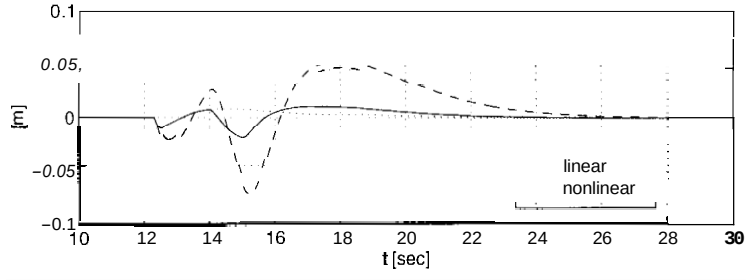

Figure 3.16: Lateral error with side wind gust of 20 m/s.

In all three cases, it is seen that Sliding Control with the nonlinear attraction term provides very robust performance. Even in the very severe case of 100% incorrect estimate of the road conditions, the peak error for the 2 m/s^2 lateral acceleration maneuver only 15 cm. This deviation is well within the effective range of the magnetic field sensors. In contrast, Sliding control with the linear attraction term is more sensitive to parameter estimation errors, for the same value of attraction gain, η.

3.5 Conclusion

From the results of the simulation study, we conclude that although a coupling between the lateral and longitudinal dynamics does exist, its effects are noticeable only at high velocities and moderate-to-high accelerations. Hence, as a practical matter, we can neglect the coupling during typical AHS applications on favorable pavement. The benefits of combined control become apparent during such transient maneuvers as lane change, entry/exit, and braking. Borrowing from the friction ellipse concept of **chapter 2,** the effective combined control regime can be graphically denoted by the following figure.

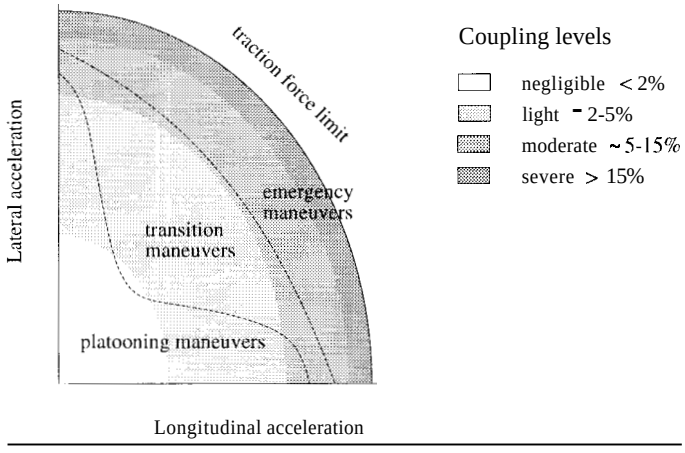

Figure 3.17: Lateral and longitudinal operational regimes.

Unfortunately, the lack of adequate high-speed test facilities makes it difficult to experimentally verify the ellipse of Figure 3.17. Currently, PATH has available for combined maneuver experiments a low-speed (< 25 m.p.h.) track and a mid-speed (–35 m.p.h.) track.

Aside from the coupling issue, we have also shown that Sliding Control offers a promising solution to the vehicle control problem. It provides the necessary level of robustness required for operations in the highly uncertain AHS environment, whether these unknowns be attributed to inertia values, road conditions, or sudden, external loads. The primary drawback to Sliding Control design is that it requires certain state measurements which are currently unavailable, *i.e.* lateral velocity. Moreover, we do not expect such measurements to be practically obtainable. Consequently, this begs the issue of nonlinear state estimation, which is not addressed in this study.

However, we can fall back on the robustness of the Sliding Controller and omit the lateral velocity in the control. This error can be lumped into the "disturbance" term. The robust performance of the Sliding Controller in the face of unknown disturbances is well known. The trade-off here is that higher gains may be required, which may result in poor ride quality. Admittedly, the issue of passenger comfort has been given scant attention in this chapter. This was a purposeful effort as we wanted to separate the problem of tracking from the problem of ride quality, since comfort becomes an issue primarily during transients, *i.e.* at line-arc intersections or during brake-throttle switching. The latter point is beyond the scope of this project, while the former is discussed in Pham (1996).

4 Longitudinal control strategies

4.1 Introduction

In contrast to most tracking problems, vehicle control for AHS has an added dimension of complexity due to the dynamic interaction among the vehicles in a certain neighborhood. For not only must each vehicle be individually stable, but we must guarantee that the group dynamics do not possess any hidden instabilities. Furthermore, this problem is rendered nontrivial for a countably infinite group. The class of such systems affected by this consideration is the so-called interconnected system (Swaroop, 1994); of which the vehicle **platoon** is a member.

In particular, we consider a coordinated collection of $n+1$ vehicles linked together by a singular purpose (Fig 4.1). The front vehicle is denoted as ***leader.*** The remaining n vehicles, called followers, are charged with: i) duplicating lead vehicle maneuvers, ii) maintaining a desired relative position. Together, these n+l vehicles comprise the platoon, the salient features of which are the coupling among the follower vehicles and their dependency upon a common leader, or more generally, a common objective.

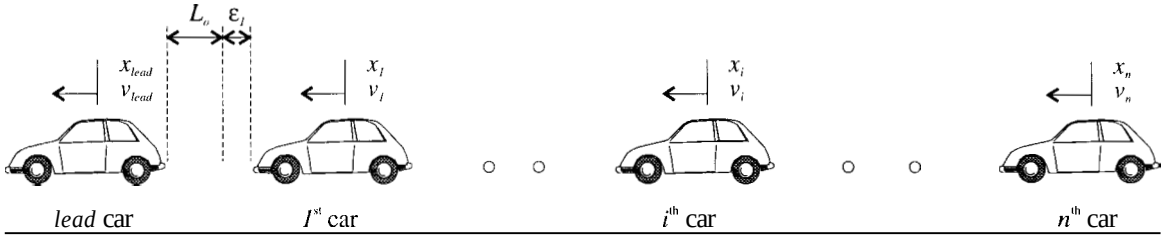

Figure 4.1: Platoon of $n+1$ vehicles.

These platoons form the basic regulation elements in the proposed AHS architecture. And as the years have progressed, there have evolved a number of different platooning strategies, *i.e.* constant spacing, headway, and safety factor vehicle-following (MacKinnon, 1975; Morag, 1974); synchronous or quasi-synchronous point-following (Wilkie, 1970; Whitney and Tomizuka, 1972); and block control (Kirk, 1973; Lang, 1975). The effectiveness of a particular choice is decided by how tightly vehicles can be packed on a given section of roadway; its cost is measured by the amount of infrastructural and hardware changes required for practical implementation; and underlying is the need for robust stability.

While the most obvious method for regulating spacing in a close-packed environment would seem to be a *vehicle-following* scheme, the associated "slinky effect" phenomenon (coined by Sheikholeslom, 1990) poses a major obstacle and weighs heavily in design considerations. In contrast stands the *point-following* scheme, whereby each vehicle is tasked with tracking its own moving reference points. This scheme can be likened to having a group of vehicles electronically tied to a moving conveyor belt. Since there are no interactions among vehicles, there exist no slinky effect. Unfortunately, this non-interaction also presents real dangers in the event of a rogue member since direct communication and sensing between vehicles are not available. Primarily for this reason, point following has fallen into almost universal disfavor.

Indeed, much of the effort in longitudinal research in recent years have been devoted exclusively to the vehicle-following approach. Among the proponents of this strategy, two particular methods enjoy equal support, *constant headway* and *constant spacing* vehicle-following:

i) *constant spacing* - desired spacing between vehicles, L_0, is fixed. This approach yields a relatively high road capacity as L_0 can be made small, typically on the order of 1 meter. However, it has been shown by Shladover that stability of the platoon is

not possible without lead vehicle information (1978). Hence, extensive inter-vehicle communication is required to avail every follower of the leader's intentions.

ii) *constant headway* - desired spacing becomes a function of vehicle velocity. The headway time, t_d, is fixed and the desired spacing is given by $H = L_0 + V.t_d$. Lead vehicle information is no longer required to guarantee stability and the need for inter-vehicle communications is eliminated. The drawback is that control effort varies inversely with the headway time. Consequently, achievable traffic capacity is diminished since t_d must be large enough (typically 0.2 sec) to prevent throttle or brake saturation (Chiu et. al. 1977; Swaroop, 1994).

A comparison of traffic throughput estimates for the two strategies are plotted for a range of cruising speeds (Fig 4.2) (Hedrick et. al., 1996).

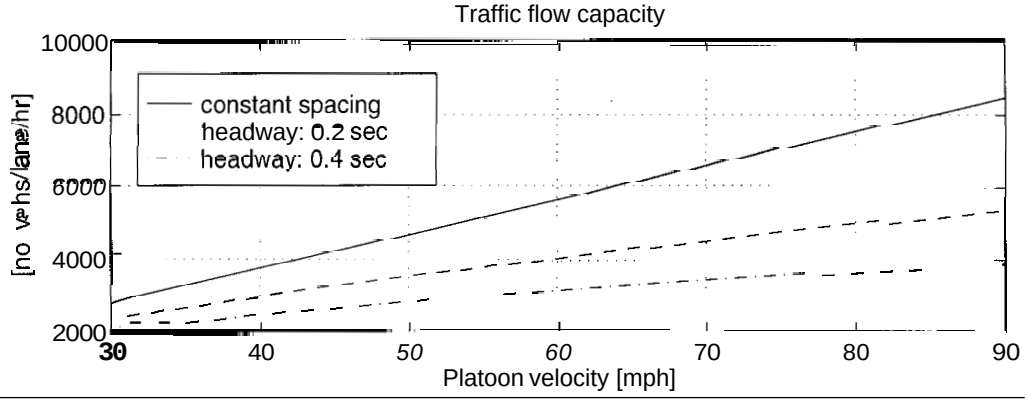

Figure 4.2: Capacity comparisons for constant spacing and constant headway strategies. *spacing:* between platoons = 76.5 m; between vehicles = 1.0 m (L_0).

As expected from the fact that headway distances must increase with increasing velocities, capacity difference between the two strategies is seen to diverge at higher speeds. At a projected highway speed of 70 mph, the difference is over 50% even with a non-conservative headway time of t_d = 0.2 sec. Hence, from a pure traffic capacity

argument, constant spacing is clearly superior. But as mentioned in (*i*), the communication costs associated with this scheme diminishes its appeal.

In this chapter, an alternative to *(i)* and *(ii)* is proposed. The proposed scheme borrows from the point-following and vehicle-following strategies by tying vehicles to both an external reference, as well as to each other. This allows for tight vehicle packing without the need for inter-vehicle communication. Rather, this hybrid scheme exploits the existing communication link between the lead vehicle and the roadside planner to reference the entire platoon to a set of "moving" magnetic markers.

Also in this chapter, the issue of platoon stability is addressed and Swaroop's string stability criteria are refined to include the definition of "uniform exponential string stability." Then, the hybrid combination of the vehicle-following and point-following schemes is shown to satisfy some proposed sufficient conditions for uniform exponential string stability. Finally, simulation results with different longitudinal control strategies are presented to provide a basis for comparison of performance and robustness.

4.2 Vehicle-following control

4.2.1 Constant spacing policy

4.2.1a No lead vehicle reference

It has been stated **(4.1)** that platoon stability is not possible in a constant spacing control strategy without lead vehicle information. To verify the truth of this claim, and to better understand the notion of stability, in the sense of platoons, it is worth examining the error dynamics between successive vehicles.

Following Swaroop, the linearized vehicle dynamics can be represented as a linear second-order system with synthetic control

$$x_i = u, \tag{4.1}$$

Under constant spacing control, error between the i^{th} and the i-1^{st} vehicles is defined as

$$\varepsilon_i \equiv x_i - x_{i-1} + L_{car} + L_0 \tag{4.2}$$

where L_0 is the desired vehicle spacing.

With no lead vehicle information, the constant spacing control law

$$u_i \equiv -k_v \dot{\varepsilon}_i - k_p \varepsilon_i \tag{4.3}$$

results in the following error dynamics between successive vehicles

$$\ddot{\varepsilon}_i + k_v \dot{\varepsilon}_i + k_p \varepsilon_i = k_v \dot{\varepsilon}_{i-1} + k_p \varepsilon_{i-1} \tag{4.4}$$

This leads to the following transfer function between $\varepsilon_i(s)$ and ε_{i-1} **(s)**

$$H(s) \equiv \frac{\varepsilon_i(s)}{\varepsilon_{i-1}(s)} = \frac{sk_v + k_p}{s^2 + sk_v + k_p} \tag{4.5}$$

From the fact that the zero of (4.5) must lie to the *left* of the right-most pole, *i.e.* $2k_p > k_v^2$ (otherwise, $\|H(j\omega)\|_\infty > 1$), it is seen that the damping between successive vehicles in constant spacing control can never be larger than the critically damped factor

$$\Rightarrow \qquad \zeta = \frac{k_v}{2\sqrt{k_p}} < \frac{\sqrt{2}}{2} \tag{4.6}$$

The effect of underdamping on the stability of the error dynamics is shown in Fig 4.3a for two platoons ($\zeta = 0.5$ and $\zeta = 0.7$) executing identical maneuvers.

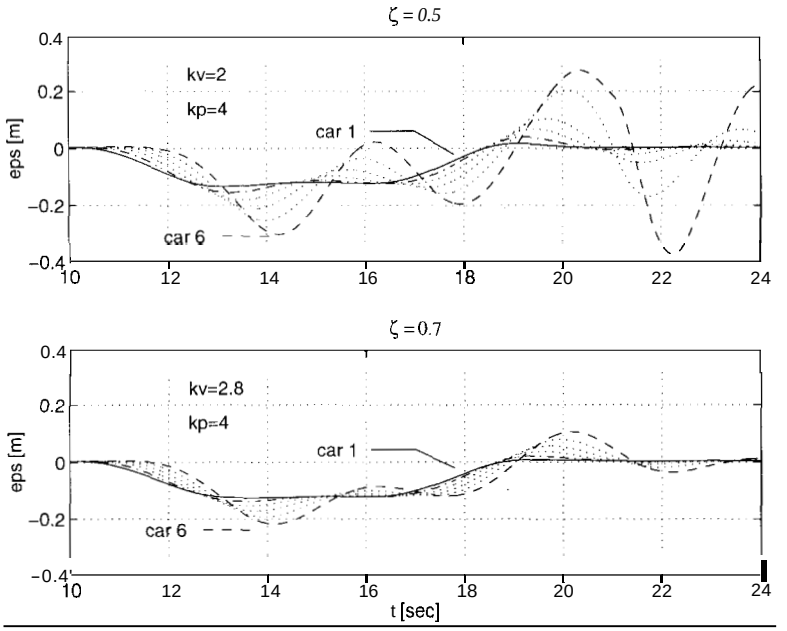

Figure 4.3a: Longitudinal spacing errors in platoon with no lead vehicle information.
control: $u_i = -k_v \dot{\varepsilon}_i - k_p \varepsilon_i$; ***velocity:*** $V_{platoon} = 45 \rightarrow 60$ mph .

The preceding plots appeal to our intuitive understanding of platoon behavior. For obviously, if the dynamics between every vehicle pair were underdamped, small perturbations at the head of the string will propagate and amplify downstream. Further, as the damping decreases, so should this "slinky effect" increase. The slinky-effect, then, serves as one meter for quantifying platoon stability. **A** different meter is provided in **section 4.4.**

In addition to error propagation, other adverse effects can be seen the control inputs (Fig 4.3b), where underdamped error dynamics lead to early throttle saturation in the case of ζ=0.5.

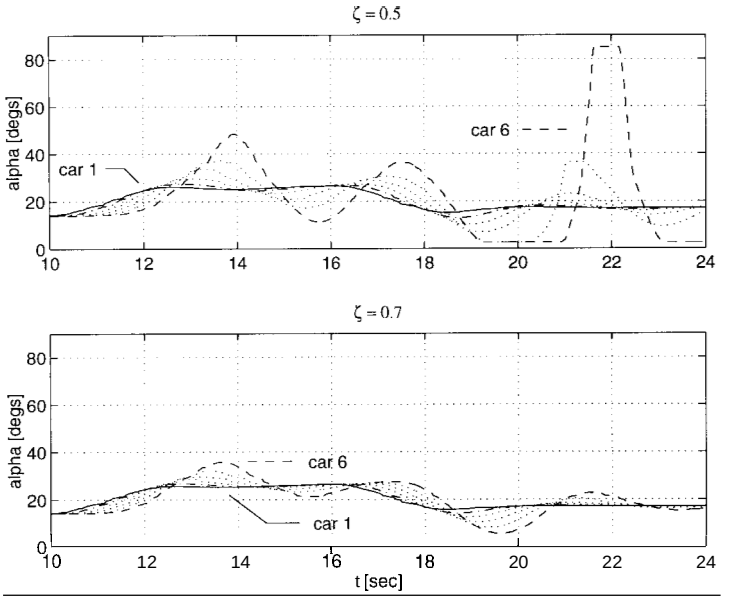

Figure 4.3b: Throttle angle inputs.

4.2.1b With lead vehicle reference

Vehicle-following is tantamount to high-speed game of "follow-the-leader." Consequently, just as we learned from our play ground experiences that it *helps* to know what the leader is doing, so can we apply this axiom to the platooning strategy. In the control sense, the "help" comes in the form of additional damping between successive vehicles in the platoon.

Consider a control of the form

$$u_i \equiv -k_v \dot{\varepsilon}_i - k_p \varepsilon_i - k_d (\dot{x}_i - \dot{x}_{lead}) \tag{4.7}$$

where the lead vehicle's velocity is available for control. Proceeding as before, the following transfer function is obtained

$$H(s) = \frac{sk_v + k_p}{s^2 + s(k_v + k_d) + k_p} \tag{4.8}$$

Thus, it is seen that by feeding back lead vehicle velocity, the denominator of the transfer function (4.8) gains added flexibility in the s-term coefficient. This extra degree of freedom can be used to increase the error damping,

$$k_p > \frac{(k_v + k_d)k_v}{2} \qquad \zeta < \frac{\sqrt{2}}{2}\sqrt{1+\frac{k_d}{k_v}} \tag{4.9}$$

Since there are only two constraints (4.9) on three parameters, the damping ratio can be made arbitrarily high by appropriate choice of k_p, k_v, and k_d. Particularly, the following choice of gains yields overdamped dynamics: $k_p = 4,\ k_v = 2,\ k_d = 2 \quad \Rightarrow \quad \zeta = 1$. Simulation results for the same maneuver as in **4.2.1** are shown for the overdamped case ($\zeta = 1$).

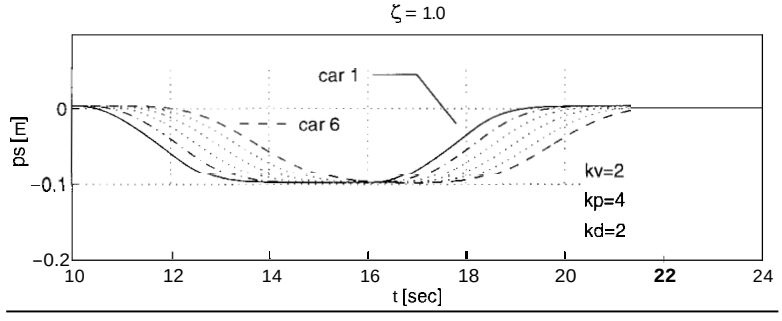

Figure 4.4: Longitudinal spacing errors in platoon with lead vehicle feedback.
control: $u_i = -k_v\dot{\varepsilon}_i - k_p\varepsilon_i - k_d(\dot{x}_i - \dot{x}_{lead})$; *velocity:* $v_{platoon} = 45 \rightarrow 60$ mph

4.2.2 Constant headway control

In contrast to the constant spacing approach, constant headway control attempts to increase the relative damping by *relaxing* the spring-dependent forces according to a velocity schedule. Under constant headway control, a "generalized" spacing error can be defined as (Ioannou et. al., 1992)

$$6; \equiv x, - x_{i-1} + L_o + t_d \dot{x}_i \tag{4.10}$$

In order to obtain exponential decay of the error ($\dot{\delta}_i = -\lambda\delta_i$), choose the control as (Xu, 1994)

$$u \equiv -\frac{\dot{x}_i - \dot{x}_{i-1} + \lambda\delta_i}{t_d} \tag{4.11}$$

The control (4.12) leads to error dynamics between vehicles of the form

$$t_d\ddot{\delta}_i + (1+\lambda t_d)\dot{\delta}_i + \lambda\delta_i = \dot{\delta}_{i-1} + \lambda\delta_{i-1} \tag{4.12}$$

with the associated overdamped transfer function

$$H(s) = \frac{s+\lambda}{(t_d s+1)(s+\lambda)} = \frac{1}{t_d s+1} \tag{4.13}$$

However, note that the control effort (4.11) is inversely proportional to headway time, t_d. This is the biggest drawback to the constant headway law for it implies a finitely large headway times to insure that the control remains bounded. Recall that increased headway times imply decreased road capacity.

4.3 The case for hybrid vehicle-following, point-following control

In the previous section on constant spacing control, the need for reference vehicle information was established. This information is made available by having the lead vehicle radio its velocity back to every platoon member. This approach yields two distinct weaknesses. One, it adds an extra layer of communication. The cost comes as increased load on the radios and a limit on the practical length of the platoon since the broadcast power of a vehicle is necessarily limited. Two, there is no direct measurement of the relative closing rate between the lead and i^{th} vehicles. Rather, the values are but indirect estimates based on wheel speed measurements -- estimates that are sensitive to parameter errors or excessive wheel slip.

To appreciate the effect of velocity estimation errors on platoon performance under (4.7), consider the following platoon simulation for wet road conditions where tire characteristics differences can be aggravated -- leading to larger estimation errors. Observer that the stability of the platoon has now been destroyed due to a small *5%* error in lead vehicle velocity (Fig 4.5).

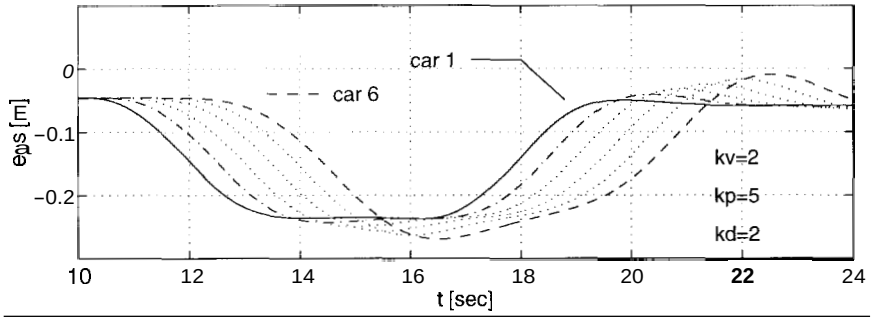

Figure 4.5: Constant spacing control with lead vehicle velocity -*5%* error on v_{lead}

A proposition:

In order to ensure a cost-effective, more robust platooning strategy, the following hybrid combination of the vehicle-following and the point-following schemes are proposed. The vehicle-follower portion provides the spring-damper interconnection between vehicles. While at the same time, the point-follower portion provides additional damping by tying the vehicles to the moving belt (Fig 4.6). Robustness derives from the fact that the platoon is referenced to an absolute velocity, rather than an estimated lead vehicle velocity. Moreover, this scheme is cost-effective since it eliminates most direct vehicle-to-vehicle communication.

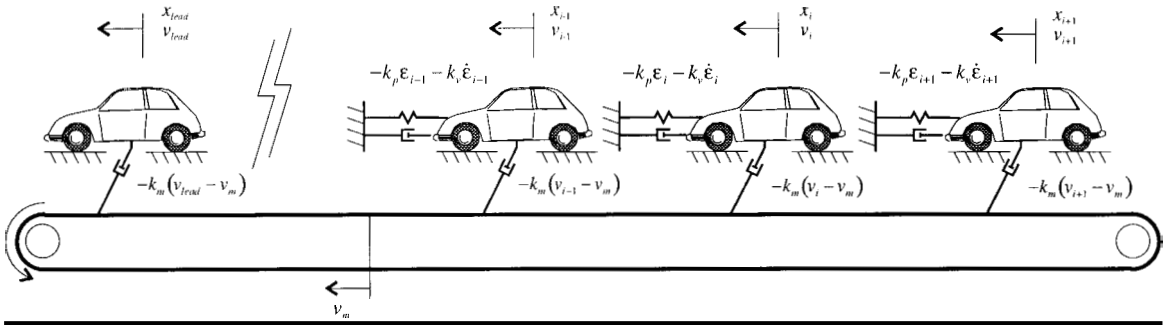

Figure 4.6: Hybrid vehicle-following/point-following platooning strategy.

To each section of roadway, a tower (called a roadside planner), is assigned the task of regulating every platoon in the area. The planner regulates each platoon by broadcasting a periodic signal at a platoon-specific frequency. This signal consists of alternating pulses of "high's'' and "low's'', with a period equal to the time desired for every vehicle in the platoon to cover the distance between successive markers.

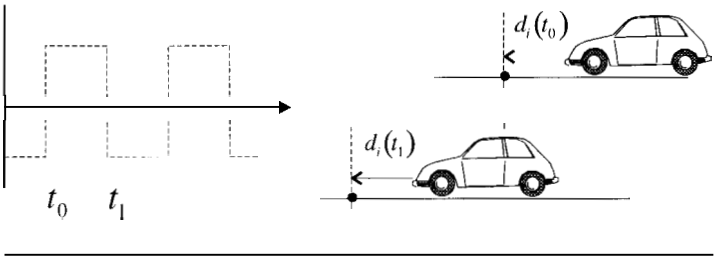

Figure 4.7: Schematic of the point-following law.

Suppose a pulse is received by vehicle i at time, *to.* Its distance from the closest marker is $d_i(t_0)$ (Fig 4.7). *Note:* this distance can be estimated by measuring the local magnetic field about the marker. At the instant of the next pulse, t_1, its distance from the next marker is $d_i(t_1)$. Then, the error between the vehicle's average velocity and the belt's "velocity" is given by (generally)

$$v_i(t_{k1}) - v_{marker}(t_k) = \frac{d_i(t_k) - d_i(t_{k-1}) + d_{marker}}{t_k - t_{k-1}} - \frac{d_{marker}}{t_k - t_{k-1}} \tag{4.14}$$

and the hybrid control can be implemented as

$$u_i(t) = -k_v\dot{\varepsilon}_i(t) - k_p\varepsilon_i(t) - k_m\left(v_i(t_k) - v_{marker}(t_{k-1})\right); \qquad t \in (t_{k-1}, t_k] \tag{4.15}$$
$$= -k_v\dot{\varepsilon}_i(t) - k_p\varepsilon_i(t) - k_m\frac{d_i(t_k) - d_i(t_{k-1})}{T_m}$$

where $T_m = t, -t_{k-1}$ is the pulse period. In the event that more than (or *less* than) one marker is encountered within one pulse period, the last term in (4.15) can be modified by

$$-k_m\frac{d_i(t_k) - d_i(t_{k-1}) + (n-1)d_{marker}}{T_{111}} \tag{4.16}$$

where *n* indicates the total number of markers encountered within the period.

From the fact that the spacing error at time, t_k, is $\varepsilon_i(t_k) = d_i(t_k) - d_{i-1}(t_k) - L_i$, the error difference from 2 successive measurements is given by

$$\varepsilon_i(t_k) - \varepsilon_i(t_{k-1}) = \left(d_i(t_k) - d_i(t_{k-1})\right) - \left(d_{i-1}(t_k) - d_{i-1}(t_{k-1})\right) \tag{4.17}$$

and the block diagram from the platoon can be represented as in Fig 4.8. Here, L_i is some nominal spacing, $L_i = L_0$ + preceding vehicle length - number of markers separating vehicles. Observe that this quantity (L_i) is unimportant since it is differenced out in (4.17).

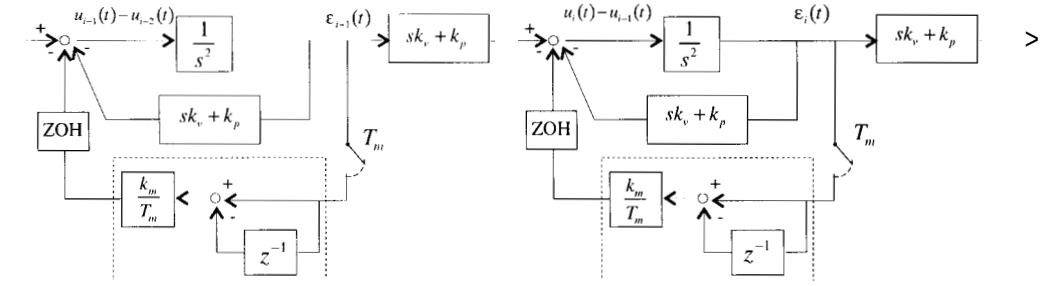

Figure 4.8: Block diagram of vehicle spacing errors.

Thus, is the hybrid nature of the feedback system evident, with the continuous-time part representing vehicle-following control and the discrete-time part representing point-following control. **As** has been shown, the continuous-time portion of (4.15) by itself does not guarantee platoon stability due to its being underdamped. To gauge the

damping effect due to the additional discrete portion, let us examine its **approximate** continuous-time representation. The following analysis is, by no means, rigorous; rather, the intent is to provide insight into the added benefits of the hybrid policy. A more formal proof of stability is presented in **section 4.5.**

The discrete block in Fig 4.8 is described by

$$G(z^{-1}) = \frac{k_m}{T_m}[1 - z^{-1}] \qquad \textbf{\textit{(4.18)}}$$

Assuming that the sampling rate is "fast" relative to the error dynamics, the approximate continuous time representation can be obtained by applying Tustin's approximation

$$\Rightarrow \qquad \hat{G}(s) = \frac{2k_m s}{(T_m s + 2)} \qquad (4.19)$$

This yields the following closed-loop error transfer function

$$\hat{H}(s) = \frac{\varepsilon_i(s)}{\varepsilon_{i-1}(s)} = \frac{T_m k_v s^2 + (T_m k_p + 2k_v)s + 2k_p}{T_m s^3 + (2 + T_m k_v)s^2 + (T_m k_p + 2k_v + 2k_m)s + 2k_p} \qquad \textbf{\textit{(4.20)}}$$

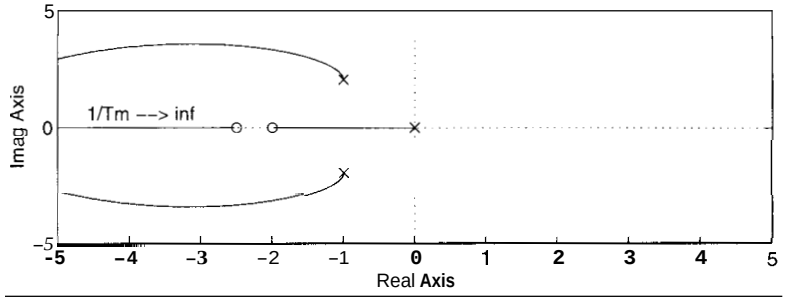

Figure 4.9: Locus of the poles of *(5.20)* as $T_m \to 0$.
($k_v = 2.0, k_p = 5.0, k_m = 2.5$)

Since T_m is small, *i.e.* $T_m << (1, k_v, k_p, k_m)$, the dominant poles (Fig 4.9) of the transfer function approach

$$p \to -\frac{k_v + k_m}{2} \pm \frac{\sqrt{(k_v + k_m)^2 - 4k_p}}{2} \qquad \textbf{\textit{(4.21)}}$$

as the dominant zero approaches

$$z \to -\frac{k_p}{k_v} \tag{4.22}$$

Hence, the situation becomes analogous to the constant spacing control strategy with lead vehicle feedback. It has already been shown that this scheme yields overdamped error dynamics. A simulation for a platoon ($\zeta = 1$) under wet road conditions with the hybrid control is presented in Fig 4.10. As the plot indicates, platoon stability in retained in the presence of velocity estimate errors.

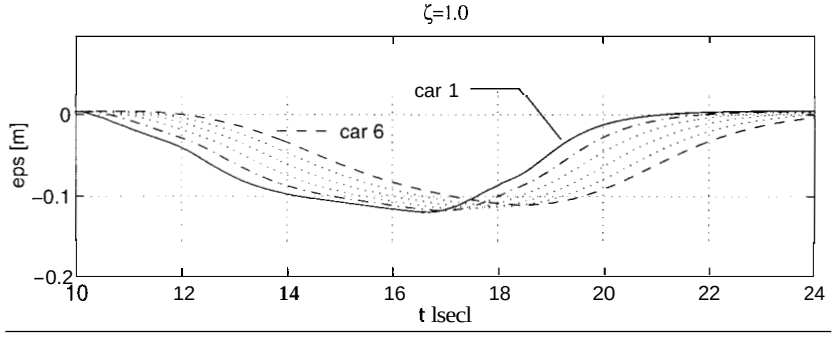

Figure 4.10: Longitudinal spacing errors in hybrid platoon scheme.
control: $u_i(t) = -k_v \dot{\varepsilon}_i(t) - k_p \varepsilon_i(t) - k_m \left[d_i(t_k) - d_i(t_{k-1}) \right] / T_m$
-5% error on v_i.

Aside from robustness to velocity estimation errors, other advantages offered by this approach include:

- Communication demands are lessened. Since the roadside signal is either "high" or "low," very little computation time is required to decode the signal content and signal integrity is much less susceptible to corruption.

- More robust to communication blackout. Consider the situation of a lead car emerging from an obstruction (tunnel, overpass, *etc.*). With the system of lead vehicle broadcast, every trailing vehicle on the other side of the obstruction loses reference information. On the other hand, with the roadside broadcast, only those vehicles inside the obstruction loses reference information.

- Safer and more efficient. Since this method places much more regulation control in the hands of the roadside planner, as opposed to a loosely autonomous platoon operation, spacing between platoons can be reduced. The planner can optimally regulate spacing since it has access to more information in a more timely manner (assuming minimal 2-way communication between lead vehicle and planner). Also, the specter of a platoon of 100 vehicles hurtling along at 70 m.p.h. towards an unseen obstruction is avoided with centralized control.

Note that this method does not require an extra layer of communication since some manner of roadside communication is already required for AHS application. This method merely requires that the broadcast information be made available to every vehicle in the platoon, rather than just the lead vehicle, albeit at a more regular frequency.

Up to this point, the discussion has centered upon a qualitative argument for the desirability of the hybrid approach. In order to advance a more rigorous treatment, the platoon dynamics should be framed entirely in the discrete realm and its virtues extolled in this domain. For assistance, we look to the string stability results found in Swaroop (1994) and Pham (1996). In the following, a proof of the stability of the hybrid platoon strategy is presented.

4.4 Stability of hybrid platooning scheme

The hybrid system was seen to consist of two distinct parts: continuous and discrete. In actual practice, the controller is implemented digitally, yielding a discrete, multi-rate sampled system. Allowing that the sampling is synchronized, with $mT_c = T_m$, where T_c is the period of the vehicle-following loop, T_m is the period of the point-following loop, and *m* is some integer which varies according to the velocity, the block diagram in Figure 4.8 can be modified as

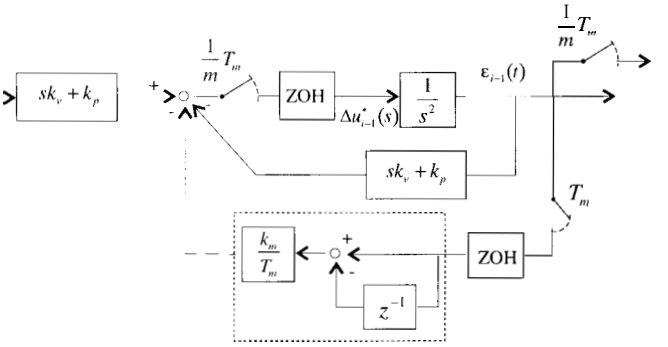

Figure 4.11: Block diagram of multi-rate sampled platoon.

From Figure 4.11, it is seen that problem complexity is dramatically increased with digital implementation. It remains possible to introduce an input-output relation between $\varepsilon_i(z)$ and $\varepsilon_{i-1}(z)$ by substituting $s = 2(z-1)/T_c(z+1)$. However, the resulting cumbersome expression blunts any insights. Instead, it may be more meaningful to study the pulse response of the sampled-system obtained from numerical simulations (Fig 4.12).

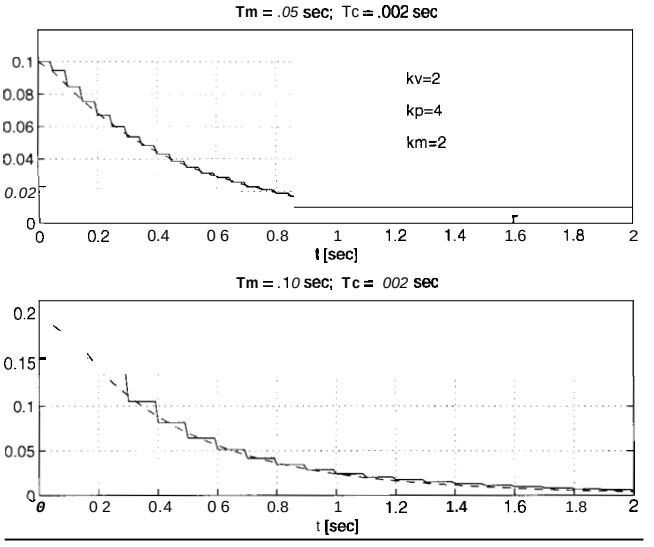

Figure 4.12: Pulse response of hybrid platoon;
predicted [- - $T_m \; .h(t)$] vs. simulated [— $\hat{h}(k)$].
$\|h(t)\|_1 = 1.0$. $\left\|\hat{h}(k)\right\|_1\Big|_{T_m=.05s} = 1.048$, $\left\|\hat{h}(k)\right\|_1\Big|_{T_m=.10s} = 1.098$

The pulse response of Fig 4.11 for two different sampling times is shown against the (*normalized*) impulse response of the approximate continuous system (4.20). It is seen that the sampled pulse response follows the predicted impulse response fairly well over a range of sampling periods. However, the *1-norm* exceeds unity by increasing margin as the sampling period becomes large -- which is not sufficient to guarantee weak string stability.

4.4.1 Hybrid control with absolute position reference

From prior results in constant spacing control, it is known that the impulse response of (4.23) can be made less than unity by including lead vehicle position. But again, extensive intervehicle communication is required to implement this policy as each vehicle has to periodically communicate its relative position to its immediate follower

$$x_i - x_{lead} + \sum_{j=1}^{i} L_j = \sum_{j=1}^{i} \varepsilon_j \tag{4.24}$$

Not only is this method cumbersome, it also introduces large lags in the error dynamics due to communication propagation delays.

With the hybrid platooning scheme, however, reference position information can be included without the need for periodic vehicle-to-vehicle communication. Suppose that the i^{th} vehicle measures its distance from the closest marker at time, $t = 0$. Simultaneously, it receives from the preceding vehicle, the error partial sum, $\omega_{i-1}(0)$. Define as the vehicle's desired spacing relative to the marker $\forall\, t \geq 0$,

$$D_i \equiv d_i(0) - \omega_i(0) = d_i(0) - \omega_{i-1}(0) - \varepsilon_i(0) \tag{4.25}$$

Then, as the vehicle moves up or down markers relative to the belt, the desired distance can be incremented or decremented, accordingly, by

$$D_i' = D_i - (n-1)d_m \tag{4.26}$$

Again, it is stressed that this strategy does not place undue hardship upon the communications because the error partial sums need to be transmitted but once -- at time $t = 0$.

The control law

$$u_i(t) = -k_v \dot{\varepsilon}_i(t) - k_p \varepsilon_i(t) - k_m \frac{d_i(t_k) - d_i(t_{k-1}) + (n-1)d_m}{T_m} - k_s\left(d_i(t_k) - D_i'\right) \tag{4.27}$$
$$t \in (t_{k-1}, t_k]$$

leads to the following control difference equation

$$u_i(t) - u_{i-1}(t) = -k_v \dot{\varepsilon}_i(t) - k_p \varepsilon_i(t) - \frac{k_m}{T_m}\left(\varepsilon_i(t_k) - \varepsilon_i(t_{k-1})\right) - k_s \varepsilon_i(t_k) \tag{4.28}$$
$$+ k_v \dot{\varepsilon}_{i-1}(t) - k_p \varepsilon_{i-1}(t)$$

since

$$\left(d_i(t_k) - D_i'\right) - \left(d_{i-1}(t_k) - D_{i-1}'\right) = \left(d_i(t_k) - d_{i-1}(t_k)\right) - \left(d_i(t_0) - d_{i-1}(t_0)\right) - \varepsilon_i(t_0) \tag{4.29}$$
$$= \varepsilon_i(t_k)$$

As before **(section 4.3**), the issue of stability is broached by our first examining the approximate continuous dynamics. Under (4.27), the transfer function of the discrete block is

$$\hat{G}(s) = \frac{2k_m s}{(T_m s + 2)} + k_s \tag{4.30}$$

This leads to the overall transfer function between and ε_i **(s)** and ε_{i-1} **(s)**

$$H(s) = \frac{T_m k_v s^2 + (T_m k_p + 2k_v)s + 2k_p}{T_m s^3 + (2 + T_m k_v)s^2 + (T_m k_p + T_m k_s + 2k_v + 2k_m)s + 2(k_p + k_s)} \tag{4.31}$$

It can be shown that (4.31) can be made overdamped, *i.e.* the impulse response does not change signs. Then

$$\|h(t)\| = \hat{H}(0) = \frac{k_p}{k_p + k_s} < 1, \quad \forall\, k_s > 0 \tag{4.32}$$

and it is clear that the "approximate" dynamics are uniform exponential string stable following Pham (1996).

The pulse response of the sampled platoon is compared against the predicted impulse response of (4.31) in Fig 4.13 for $T_c = 0.002s$, $T_m = 0.05$s.

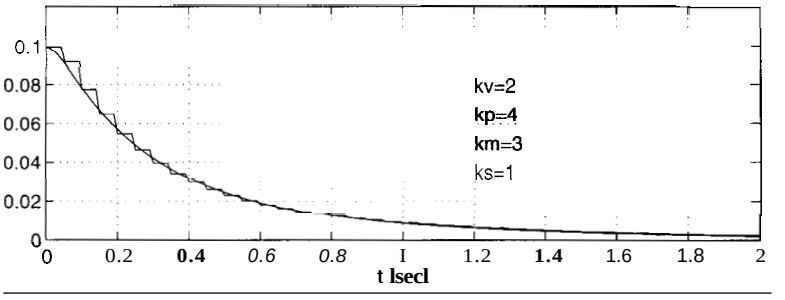

Figure 4.13: Pulse response of hybrid platoon with reference position information.
$\|h(t)\|_1 = 0.8, \quad \|\hat{h}(k)\|_1 = 0.839.$

Hence, since the sampling frequency ($1/T_c$ = 20 Hz) of Fig 4.13 is greater than twice the platoon bandwidth, $\omega_c \approx 0.5$ Hz, the platoon is uniform exponential string stable.

4.4.2 Hybrid control with preview

While much has been made of the string stability property of the hybrid platoon strategy, there has, as yet, been little attention paid to the quality of the ride and the individual tracking performance. The issue of comfort is raised since the commanded marker-encounter rates must necessarily be finitely quantized. Consequently, transition between velocities must occur as a series of jumps (Fig 4.14); the size of which has a

direct bearing on passenger comfort. The commanded velocity shown in Fig 4.14 corresponds to marker rates incremented with 1ms resolution.

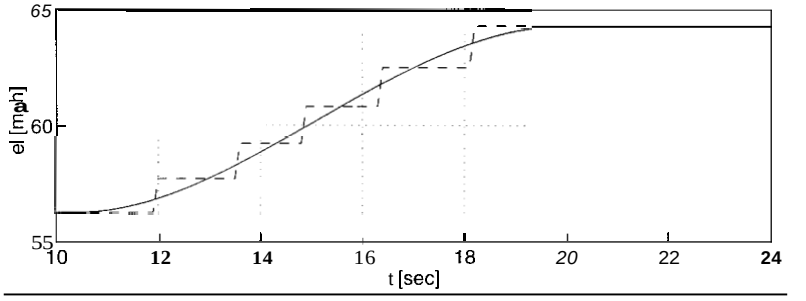

Figure 4.14: Commanded marker velocity *v.s.* desired velocity - - v_{marker}; —— v_{des}.

With preview information, however, the controller can be designed to chart a smooth course between the velocity transitions. Moreover, it is also argued that preview will allow for tighter spacing regulation since it allows for anticipation action. This preview need plays directly into the strength of the hybrid architecture since this scheme lends itself to preview with very little extra communication cost.

Suppose that the planner broadcasts the future desired marker-encounter rate at the present time. The onboard computer stores the information and the internal clock synchronizes the simulated broadcast at a later time. Thus, at any time t_k, the controller knows the reference command up to a time, $t_k + \mathbf{At}$, where the delay, **At** is uniform over all vehicles and is chosen large enough so as to ensure that instructions for at least the next *m* number of markers will be received at typical freeway speeds.

In Fig 4.14, the smooth curve represents the fictitious desired velocity generated by the controller with a 10s preview window. The desired velocity plotted here is a 4^{th}-order polynomial

$$v_{des} = a_4(t-t_i)^4 + a_3(t-t_i)^3 + a_2(t-t_i)^2 + a_1(t-t_i) + a_0 \tag{4.33}$$

satisfying the following conditions

$$
\begin{aligned}
v_{des}(t_i) &= v_{marker}(t_i) \\
v_{des}(t_f) &= v_{marker}(t_f) \\
\frac{d}{dt} v_{des}(t)\Big|_{t=t_{ii}} &= \frac{d}{dt} v_{des}(t)\Big|_{t=t_f} = 0 \\
\int_{t_i}^{t_f} v_{des}(t)dt &= x_{marker}(t_f) - x_{marker}(t_i)
\end{aligned}
\tag{4.34}
$$

where t_i is some predetermined time before the first velocity change is encountered. Likewise, t_f is some predetermined time after the last velocity change is detected. In the event that a velocity transition maneuver lasts longer than the preview window, v_{des} can be computed up to the limit of the preview horizon and regularly updated at some agreed-upon interval: say, every 1/4 of the preview length.

The boundary conditions in (4.34) will, of course, have to be modify accordingly. Let t_2 be the time of the last detectable velocity change, and let t_1 be the time of the next-to-last velocity change. Then, the boundary conditions can be modified as

$$
\begin{aligned}
v'_{des}(t_{now}) &= v_{des}(t_{now}) \\
v'_{des}(t_f) &= v_{marker}(t_1); \qquad\qquad t_f = (t_1 + t_2)/2 \\
\frac{d}{dt} v'_{des}(t) &= \frac{d}{dt} v_{des}(t) \\
\frac{d}{dt} v'_{des}(t)\Big|_{t=t_f} &= \frac{v_{marker}(t_2) - v_{marker}(t_1)}{t_2 - t_1} \\
\int_{t_{now}}^{t_f} v'_{des}(t)dt &= x_{marker}(t_f) - x_{marker}(t_{now})
\end{aligned}
\tag{4.35}
$$

where $v'_{des}(t)$ is the new desired velocity.

The platoon can be made to track the desired velocity within the hybrid architecture by manipulating the computed marker spacing. As before, let the vehicle measure its distance from the closet marker at time, t_{k-1}. At time t_k, the error between the vehicle's average velocity and the average v_{des} is

$$
v_i(t_k) - v_{des}(t_k) = \frac{d_i(t_k) - d_i(t_{k-1}) + d_m}{t_k - t_{k-1}} - \frac{\int_{t_{k-1}}^{t_k} v_{des}(t)dt}{t_k - t_{k-1}} \tag{4.37}
$$

Likewise, the desired reference position, D_i', in (4.26) can also be changed by

$$D_i'(t_k) = D_i - (n-1)d_m + \int_{t_{k-1}}^{t_k} v_{des}(t)dt - d_m \tag{4.38}$$

Note that since v_{des} is independent of vehicle index, the use of (4.37-8) does not change the string stability results of the previous section. The use of the control law

$$u_i(t) = -k_v\dot{\varepsilon}_i(t) - k_p\varepsilon_i(t) - \frac{k_m}{t_k - t_{k-1}}\left\{v_i(t_k) - v_{des}(t_k)\right\} - k_s\left\{d_i(t_k) - D_i'(t_k)\right\} \tag{4.39}$$

results in the platoon performance in Fig 4.15.

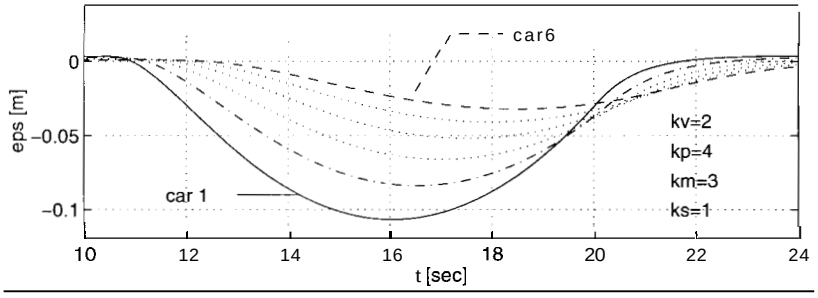

Figure 4.15a: Spacing errors of hybrid platoon with reference position and velocity information.

As the pulse response in Fig 4.13 ($\left\|\hat{h}(k)\right\|_1 = 0.839$) would predict, it is seen that the spacing errors decay down the platoon index exponentially (Fig 4.15a). The throttle commands are shown in Fig 4.15b. The smoothness of the plots suggest a comfortable ride.

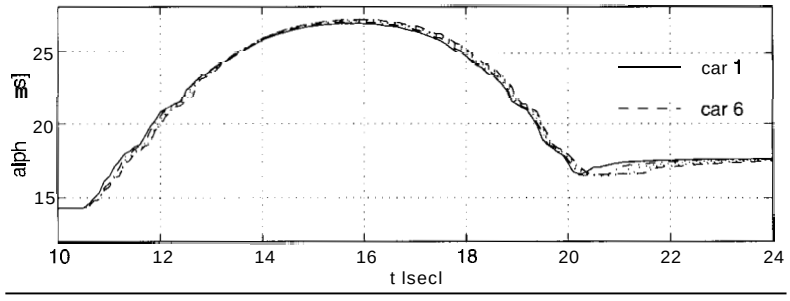

Figure 4.15b: Throttle angle inputs.

The same use of preview also improves tracking by including the desired acceleration in the control

$$u_i(t) = \dot{v}_{des}(t) - k_v \dot{\varepsilon}_i(t) - k_p \varepsilon_i(t) - \frac{k_m}{t_k - t_{k-1}} \left\{ v_i(t_k) - v_{des}(t_k) \right\} - k_s \left\{ d_i(t_k) - D_i'(t_k) \right\} \qquad (4.40)$$

where

$$v_{des} = 4a_4 (t - t_i)^3 + 3a_3 (t - t_i)^2 + 2a_2 (t - t_i) + a_1 \qquad (4.41)$$

is the acceleration corresponding to the desired velocity found in (4.33). The use of (4.40) leads to the performance in Fig 4.16.

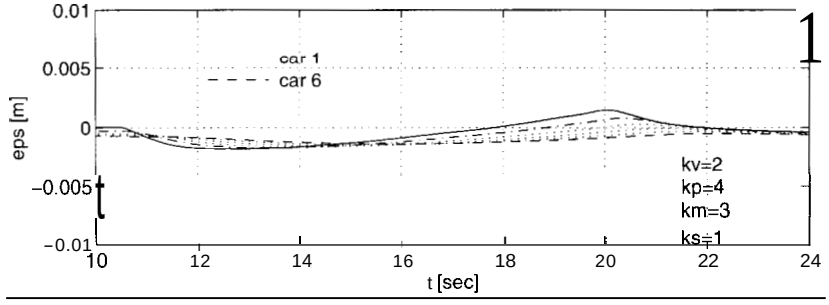

Figure 4.16: Spacing errors of hybrid platoon with reference position, velocity and acceleration information.

Observe that, with addition of reference acceleration in the control, the spacing error becomes almost negligible.

4.5 Conclusion

The proposed hybrid platoon strategy is a natural, straight-forward extension of previous works in vehicle-following and point-following control; more importantly, it is an intuitive approach that appeals on several levels. The most obvious benefit derives from the hardware redundancy provided by its using both radar and magnetic markers as

reference for the platoon member. This redundancy diminishes the possibility of catastrophic failure due to equipment malfunction. Of course, the same security margin may be achieved with back-up radars. However, it is less palatable since the magnetic system is already provided for lateral referencing; hence, the cost of redundancy is free.

On another level, the advantages of the hybrid strategy can be found in its diminished communications load. Instead of requiring regular information broadcasts (lead vehicle acceleration and velocity, and preceding vehicle acceleration and accumulated error) as in the current vehicle-following scheme, the hybrid scheme needs but a regular "heartbeat" pulse from a wayside regulator. Since this hi-lo beat contains much less information, it is much more quickly processed and is inherently more robust against corruption or loss. Moreover, since the talk occurs between roadside and platoon, rather than between vehicles, communications delays become negligible. Consequently, transmission time is no longer at issue and limits on platoon lengths are removed.

Yet, perhaps the hybrid strategy attracts strongest when it pulls at our intuitive appreciation of structure and regimen. To draw an analogy, vehicle-following control can be likened to a loosely disciplined marching band. Each vehicle attempts to follow its immediate predecessor, while striving to keep rhythm with the lead vehicle. There is, however, no conductor. Hence, there can be no guarantee of precision. In other words, platoon velocity cannot be strictly regulated. This increases the risk of collision with other platoons on the same highway due to non-uniform velocities. To minimize the chance of collision, the platoons will have to be kept sufficiently far apart. What's more, the very stability of the stability is affected by how accurately the lead vehicle estimates its motion.

On the other hand, point-following control is analogous to an ensemble of soloists under central direction. Here, the tendency is to focus on the beat to the exclusion of all else. Consequently, harmony of the group is sacrificed at the expense of individual perfection. The implication for the point-following control is that individual collisions

may occur since the dynamics between vehicles are disregarded. Indeed, even small constant velocity mismatches between two vehicles will result in a crash over time.

Conversely, the hybrid scheme benefits from both the teamwork mentality of the marching band and the precision provided by the conductor. Thus, are the disadvantages of vehicle and platoon stability overcome. This point has been successfully demonstrated by analysis and simulations. However, experimental verification remains a problem as PATH currently has only one vehicle outfitted with the necessary hardware. In the following chapter, we continue with the theme of hybrid control objectives with regard to the lateral control problem.

5 Lateral control strategies

5.1 Introduction

It is an indisputable maxim, handed down through the ages by those ancient keepers of driving lore, that the surest way to maintain lateral position relative to the lane center is to aim the vehicle at some "look-ahead" point. Add to this, a corollary: "The higher the speed, the larger the look-ahead distance." These sage words have served as a constant and faithful guide to the legions of drivers who have plied our roads and byways. Yet, the magnetic referencing system proposed for lateral regulation in the AHS architecture seems to fly in the very face of this accepted, time-tested truth. Indeed, automatic lateral control utilizing this so-called "look-down" (Guldner et. al., 1996) referencing system has been likened to a human's steering by peering through the vehicle floorboard (Tomizuka, 1992).

In this chapter, the consequences of utilizing such a look-down referencing are investigated and the drawbacks are detailed. Particularly, the resulting underdamped internal yaw dynamics are shown to impose severe performance limitations and may jeopardize lateral stability at high speeds and/or low road adhesion values. In an effort to redress these shortcomings, this chapter proposes a hybrid lateral control scheme which encompasses both look-ahead and look-down sensing.

Within the context of the PATH architecture, look-ahead information can be provided by the angle offset (or azimuth angle) of the longitudinal radar signal . Narendran and Hedrick (1994) and Pantarotto and Hedrick (1995) have demonstrated the possibility of achieving lateral regulation via azimuth angle referencing in a platoon environment (Fig 5.1). The primary control objective in this heading angle strategy is to

keep each vehicle pointed at its immediate predecessor in a manner similar to a string of boxcars' following the lead locomotive. However, this method is sensitive to accumulated lateral errors; and hence, it is not practical as a primary, or stand-alone, lateral control scheme. But when combined with the look-down lane marker following control, the tandem strategy guarantees acceptable yaw dynamics along with lateral string stability. The efficacy of the hybrid lateral control strategy is demonstrated in simulations provided at the end of the chapter.

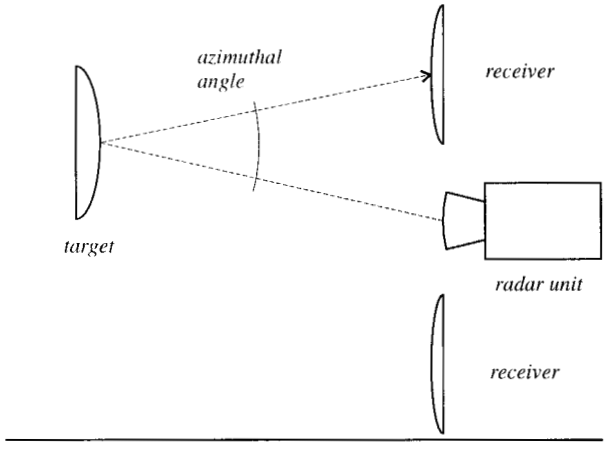

Figure 5.1: Azimuth angle reading.

5.2 Lane-following control

Since the control objective of this approach is to regulate $y_s = 0$, the vehicle's yaw motion becomes hidden from an input-output $(6 - y_s)$ perspective. Hence, in order to analyze this internal behavior, it is important to explore the dynamic relationship between y_s and ψ. Since the steering control appears upon the second differentiation of the lateral position, the following Laplace domain representation may be noted,

$$s^2 y_s = sV_y + sV_x\tilde{\psi} + s^2 d_s\psi \tag{5.1}$$

where V_z is assumed constant; zero initial conditions are also assumed. Additionally, in order to reduce notational complexity, let $\psi_{rd} \equiv 0$, *i.e.* $\tilde{\psi} = \psi$.

Further, from the linear bicycle model, we have that

$$\left[s + \frac{2\mu\left(C_{s_f} + C_{s_r}\right)}{mV_x}\right]V_y = -V_x\psi + \frac{2\mu C_{s_f}}{m}\delta \tag{5.2}$$

$$\delta = \frac{I_z}{2l_f\mu C_{s_f}}\left[s^2 + \frac{\mu\left(l_f^2 C_{s_f} + l_r^2 C_{s_r}\right)}{I_z V_x}\right]\psi \tag{5.3}$$

Together, (5.1-3) combine to yield the following input-output relation between the lateral error and the yaw dynamics

$$\frac{\psi}{Y_s} = H(s) \tag{5.4}$$

$$= \frac{l_f\left\{mV_x s + 2\mu\left(C_{s_f} + C_{s_r}\right)\right\}s}{V_x\left(I_z + ml_f d_s\right)s^2 + 2\mu\left\{l_f^2 C_{s_f} + l_r^2 C_{s_r} + l_f d_s\left(C_{s_f} + C_{s_r}\right)\right\}s + 2l_f V_x\mu\left(C_{s_f} + C_{s_r}\right)}$$

In turn, (5.4) implies the following damping ratio

$$\zeta = \frac{\sqrt{\mu}}{V_x\sqrt{2}}\frac{l_f^2 C_{s_f} + l_r^2 C_{s_r} + l_f\left(C_{s_f} + C_{s_r}\right)d_s}{\sqrt{l_f\left(C_{s_f} + C_{s_r}\right)\left(I_z + ml_f d_s\right)}} \tag{5.5}$$

Consequently, from (5.5), several points become clear (Fig 5.2):

i) yaw damping increases with increasing d_s;

ii) yaw damping increases with increasing road adhesion;

iii) yaw damping decreases with increasing velocity.

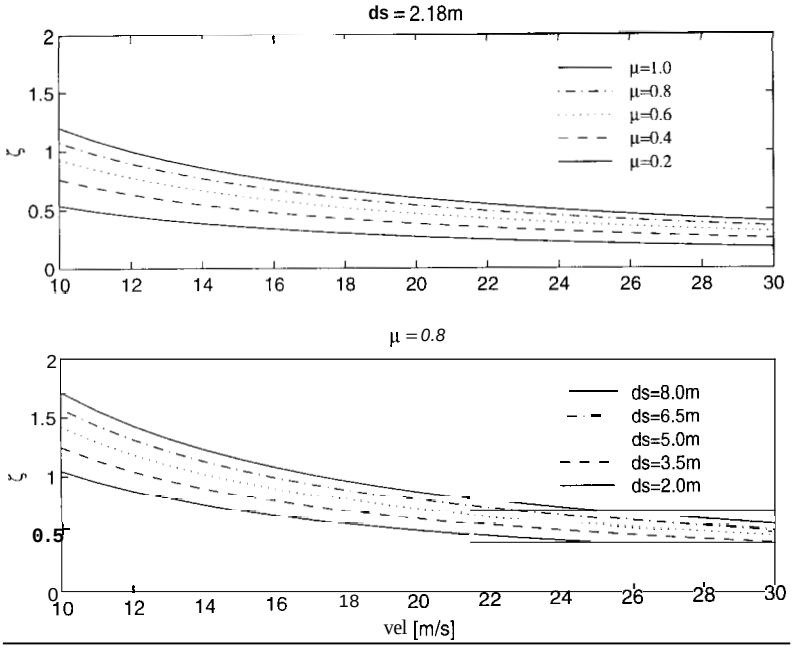

Figure 5.2: Yaw damping as a function **of** d_s, V_x, and μ.

These observations indicate that the current lane following strategy using the magnetic marker referencing system is inherently unsafe, especially at high speeds, or under adverse road conditions. Note that in order to obtain adequate damping, *i.e* $\zeta > 0.707$, with the current magnetic sensor placement ($d_s = 2.18\text{m}$), it is required that speeds be kept under 15 m/s for dry road operations ($\mu = 0.8$). For operations on wet road ($\mu = 0.4$), the speed must be scaled back to 10 m/s. The consequence of underdamped dynamics are excessive yaw motions which may saturate tire forces, or in less severe cases, cause passenger discomfort. And while it is theoretically possible to increase the available yaw damping by lengthening d_s, it is impractical to extend magnetometer placement beyond the vehicle front end -- much less to the required 10m

indicated in Fig 5.2. *Note:* The possibility of using magnetometers at both the front and rear bumpers in order to extend the effective d_s was investigated in Guldner, et al. (1996)

Simulations for a single vehicle under lane following control is shown for several values of road adhesion coefficient. The road is a straight segment; the vehicle is given an initial lateral offset displacement of 40 cm. The plant parameters, *i.e.* road adhesion coefficients, are assumed to be known by the controller in all runs. The vehicle velocity is 30 m/s, and the sensor distance is 2.18 m.

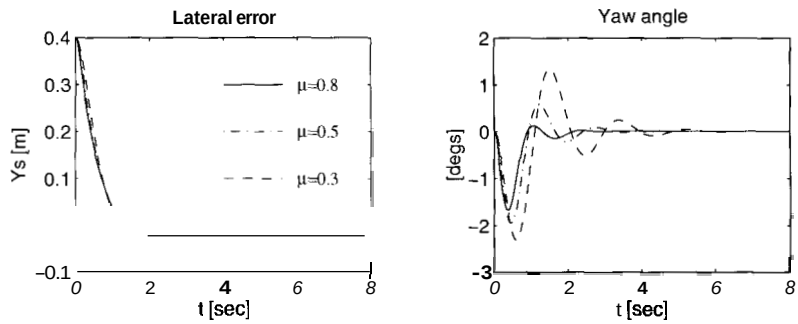

Figure 5.3: Lateral response under varying road conditions.

From Fig 5.3, note that the lateral tracking performance remains constant. The yaw performance, however, degrades severely as the quality of the road/tire interface diminishes. Again, this corroborates our earlier observation *(ii)* drawn from the damping ratio *(5.5)*.

5.3 Heading angle control

In contrast, consider azimuth angle control, where the task is to regulate $\Delta\psi = 0$. Since the primary objective here is to control the vehicle's heading, the issue of underdamped yaw motion becomes moot. However, it is easy to see that the lateral error of the following car under this control strategy depends directly upon the lateral error of the preceding car. Indeed, the lateral error of the i^{th} vehicle can be expressed as (Fig 5.4)

$$y_s^i = y_s^{i-1} - L\psi^{i-1} + R\left(\Delta\psi^i - \psi^i\right) \tag{5.6}$$

where the *superscripts* denote vehicle index, ***R*** is the intervehicle spacing, and *L* is vehicle length. Note that a straight road is once again assumed. The heading angle strategy, and the subsequent analysis, can be readily extended to curved sections of road by introducing a desired offset quantity, $\Delta\psi_{des} \neq 0$ (see Narendran, 1995). The control task is then to regulate $\Delta\psi - \Delta\psi_{des} = 0$.

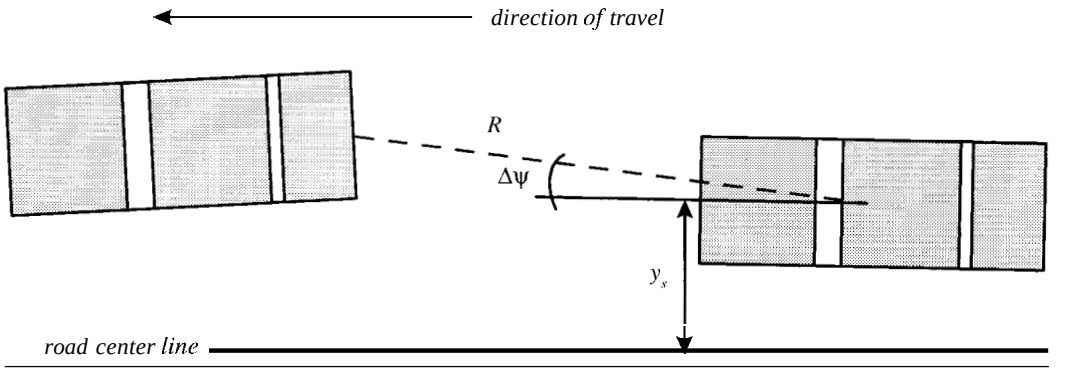

Figure 5.4: Heading angle control schematic.

Similar to the previous chapter, the lateral string stability can be analyzed by noting the following feedback law

$$\ddot{\psi}^i = -k_v\Delta\dot{\psi}^i - k_p\Delta\psi^i \tag{5.7}$$

Then, a transfer function representation between y_s^{i-1} and y_s^i can be obtained by combining eqs (5.2-3) and (5.6-7)

$$\left(s^2 + sk_v + k_p\right)\psi^i + \frac{\left(sk_v + k_p\right)}{R}y_s^i = \frac{\left(sk_v + k_p\right)}{R}\left(y_s^{i-1} - L\psi^{i-1}\right) \tag{5.8}$$

$$\Rightarrow \qquad \left(s^2 + sk_v + k_p\right)\frac{N(s)}{D(s)}y_s^i + \frac{\left(sk_v + k_p\right)}{R}y_s^i = \frac{\left(sk_v + k_p\right)}{R}\left(1 - L\frac{N(s)}{D(s)}\right)y_s^{i-1}$$

$$= \frac{D(s) - LN(s)}{D(s) + s^2 N(s)} \tag{5.9}$$

where $N(s)$ and $D(s)$ are the numerator and denominator, respectively, of transfer function (5.4) given in the previous section.

Moreover, from the fact that

$$l_f C_{s_f} + \frac{l_r}{l_f} l_r C_{s_r} + d_s\left(C_{s_f} + C_{s_r}\right) - L\left(C_{s_f} + C_{s_r}\right) < 0 \tag{5.10}$$

it is easy to check that $G(s)$ is non-minimum phase. This behavior reflects the fact that as the vehicle points to the center, its tail must necessarily swing outward. The non-minimum phase behavior of the tail is then propagated to the following vehicle.

Noting that $G(0) = 1$ and recalling that $\|g(t)\|_\infty \geq |G(0)|$, where the equality holds if and only if $g(t)$ does not change signs, we conclude that the heading angle policy does not yield a string stable solution. For clearly, a non-minimum phase $g(t)$ changes signs. Simulations results are shown for a string of 5 vehicles executing heading angle control, with initial offset error of 40 cm.

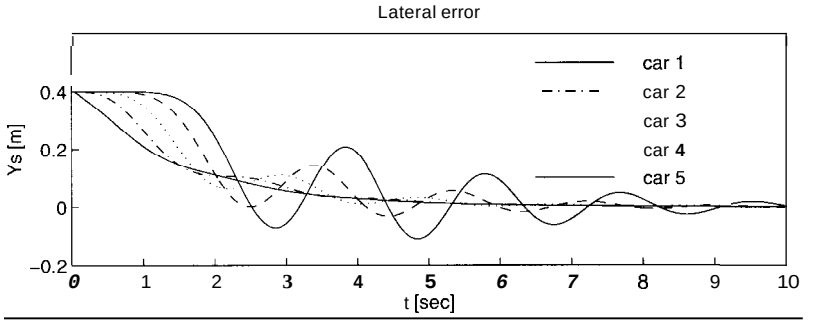

Figure 5.5: Simulation a 5-car string of under heading angle control. (R=2.0m, k_v=6.0, k_p=4.0, μ=0.5)

As predicted, the simulation results of Fig 5.5 reveal that the lateral errors are propagated with increasing amplitude down the platoon. Clearly, then, heading angle control does not yield a completely satisfactory solution.

5.4 Hybrid lane-following, heading angle control

In each of the previous two sections, the advantages and drawbacks of each lateral control strategy were discussed. Here, we play to the strengths of both (in the hopes of bolstering their weaknesses) by combining the strategies under a hybridized policy. In particular, we wish to exploit the yaw damping characteristics of look-ahead control while maintaining lateral string stability with the look-down, lane-following scheme. Once again, it is emphasized that this hybrid strategy does not require additional hardware over the currently proposed radar (for longitudinal) and magnetic marker (for lateral) referencing system in PATH's AHS architecture.

Heading angle control is analogous to tying the vehicle to the preceding vehicle's inertial frame with a torsion spring-damper. Obviously, this method cannot guarantee the primary lateral control objective, *i.e.* regulating the vehicle with respect to the road center-line. However, by combining this approach with the marker referencing system, the vehicle is effectively to road with an additional spring-damper set (Fig 5.6).

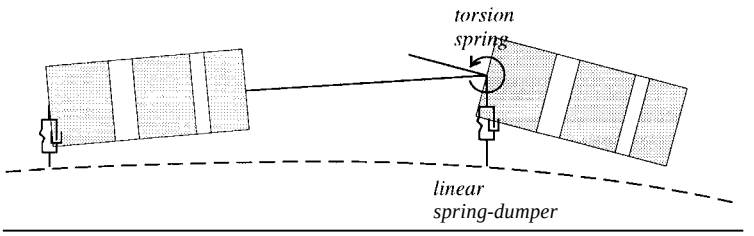

Figure 5.6: Schematic of hybrid lateral control strategy.

In order to effect the hybrid strategy, choose as the output

$$y = \frac{y_s}{R} + \frac{K_\psi \Delta\psi}{R} \tag{5.11}$$

where K, is the relative weighting gain chosen to provide a satisfactory trade-off between the lateral position and yaw angle control objectives. For the following stability analysis, the output feedback control law,

$$u_i = -k_v \dot{y}^i - k_p y^i, \tag{5.12}$$

is considered.

5.4.1 Yaw damping

The dynamic relationship between output and vehicle yaw under hybrid control can be analyzed in a manner similar to **Sec 5.2.** By setting $y_s^{i-1} = 0$, $\psi^{i-1} = 0$, observe that (5.6) leads the following relation

$$\Delta\psi^i = \frac{\left(y_s^i + R\psi^i\right)}{R} \tag{5.13}$$

This, in turn, leads to

$$y^i = \frac{y_s^i}{R} + \frac{K_\psi\left(y_s^i + R\psi^i\right)}{R^2} \tag{5.14}$$

$$\Rightarrow \qquad y^i = \frac{\left(R + K_\psi\right)D(s) + RK_\psi N(s)}{RN(s)}\psi^i$$

$$\Rightarrow \qquad \frac{\psi^i}{y^i} = \frac{RN(s)}{\left(R + K_\psi\right)D(s) + RK_\psi N(s)} \tag{5.15}$$

From (5.15) and (5.4), the following damping ratio can be obtained

$$\zeta = \frac{\sqrt{\mu}}{V_x\sqrt{2}} \frac{\left(l_f^2 C_{s_f} + l_r^2 C_{s_r}\right) + l_f\left(C_{s_f} + C_{s_r}\right)\left(d_s + \dfrac{RK_\psi}{R+K_\psi}\right)}{\sqrt{l_f\left(C_{s_f} + C_{s_r}\right)\left\{I_z + ml_f\left(d_s + \dfrac{RK_\psi}{R+K_\psi}\right)\right\}}} \tag{5.16}$$

A comparison of (5.16) with (5.5) reveals that the damping has now gained additional freedom in the heading angle gain, K_ψ. This implies that the more control emphasis we place on the heading angle, $\Delta\psi$ (as opposed to the lateral error, y_s), the greater the amount of yaw damping available for given V_x, d_s, and μ. **A** plot of the yaw damping is given in Fig 5.7 below.

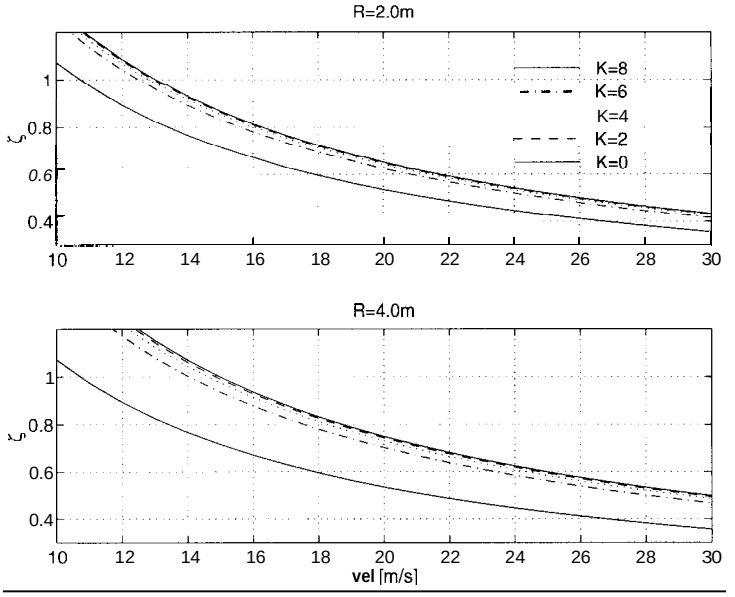

Figure 5.7: Yaw damping as a function of K_ψ, V_x, and R. (d_s=2.18m, μ=0.8)

The plots indicate that as the intervehicle spacing (R) increases, the benefits of adding heading control increases. For a value of R=2.0m, hybrid control increases the yaw damping by over 25% over pure lane keeping control. For a value of R=4.0m, the damping is increased by over 40%.

5.4.2 Lateral string stability

We choose, as the starting point for lateral stability analysis of the platoon, the output feedback law of (5.14),

$$\begin{aligned} \ddot{\psi}^i &= u^i \\ &= -k_v \dot{y} - k_p y \end{aligned} \tag{5.17}$$

This, along with (5.11), yields the following Laplace representation

$$s^2 \psi^i = -\left(sk_v + k_p\right)\left\{\frac{y_s^i}{R} + \frac{K_\psi}{R^2}\left(y_s^i + R\psi^i - y_s^{i-1} + L\psi^{i-1}\right)\right\} \tag{5.18}$$

By utilizing the relationship between $y_s - \psi$ (5.4), the following transfer function between the lateral errors of the i^{th} and i-1^{st} vehicles can be obtained

$$\frac{y_s^i}{y_s^{i-1}} = \frac{K_\psi D(s)\left(sk_v + k_p\right) - LN(s)}{D(s)\left(R + K_\psi\right)\left(sk_v + k_p\right) + RN(s)\left(Rs^2 + sk_v + k_p\right)} \tag{5.19}$$

It can be shown, at least numerically, that the impulse response of (5.19) can be made smaller than unity by appropriate choice of K_ψ. Particularly, the following impulse response can be obtained for $K_\psi = 2.0$ (Fig 5.8).

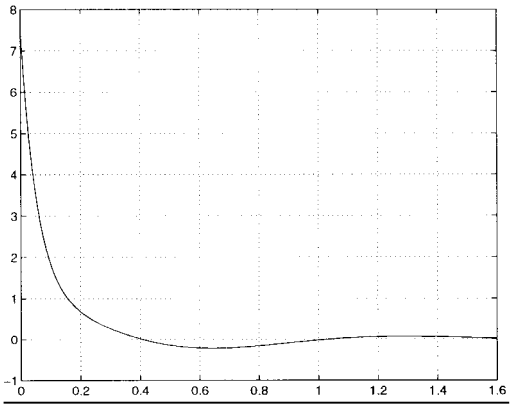

Figure *5.8:* Impulse response of (5.19).
(R=2.0m, k_v=4.0, k_p=4.0, μ=0.8)

Since the impulse response given by Fig 5.8 changes signs, a straightforward calculation of $\|h(t)\|_\infty$ is not possible. However, a numerical calculation reveals that $\|h(t)\|_\infty = 0.7$, and it is concluded that lateral string stability is possible.

Simulation results are detailed in Fig 5.9 below for a platoon of *5* vehicles executing hybrid lateral control. The parameters are the same as for Fig *5.5* in **sec 5.3.** The lateral errors are shown in the left panel, while the yaw responses are shown in the right panel.

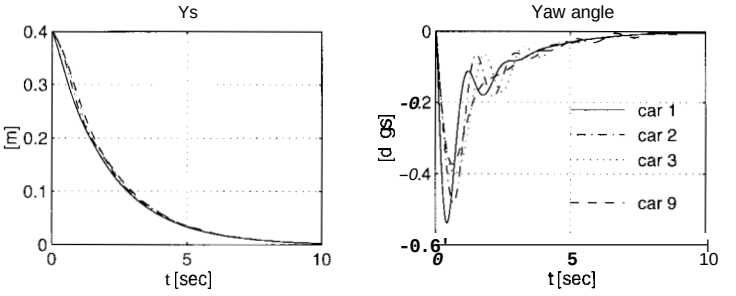

Figure *5.9:* Simulation of 5-car platoon under hybrid lateral control.
(R=2.0m, k_v=4.0, k_p=4.0, μ=0.8)

Observe that lateral errors do not amplify down the platoon. Furthermore, note that the maximum yaw angle in Fig 5.9 is less than a third of the magnitude given by a lane following strategy (Fig 5.3).

5.5 Conclusion

The preceding sections' results indicate that significant improvements in transient performance of the lane marker following strategy can be obtained by including the

relative vehicle heading angle in the control law. Moreover, it was also shown (analytically) that this improvements increase with larger inter-vehicle separation distance. The simulation study demonstrate noticeably less oscillatory yaw behavior even with a modest separation distance of 2 *m*. While not shown, a less aggressive separation distance of 4 *m* results in even better behaved yaw behavior, as predicted by the plot of yaw damping in Fig 5.7.

Perhaps just as importantly, it is argued that by combining the two lateral control objectives, a degree of redundancy is built into the system. This provides greater assurance against catastrophic failure in the case of breakdown of one of the referencing systems – whether it be a result of mechanical failure, false readings, or in the case of the magnetic referencing system, large local anomalies in the earth's magnetic field. Finally, it is stressed that this redundancy may be obtained at no extra hardware costs, in the context of the pre-existing independent longitudinal and lateral referencing systems.

Chapter 6

Conclusion

Whereas past AHS control-layer research assumed independent dynamics in the lateral and longitudinal directions, this project represents the first in-depth effort at integrated vehicle modeling and control for combined maneuvers. It was determined that the lateral and longitudinal coupling becomes apparent even at moderate lateral and longitudinal maneuvers (*i.e.* < 2 m/s^2) and that the performance of the independent lateral and longitudinal controllers degrades significantly in the presence of this coupling. Additionally, it was found that the inherent weaknesses of the longitudinal vehicle-following and lateral lane-following schemes can be easily overcome by combining their respective sensing sub-systems into a single, comprehensive reference system. Indeed, not only does this approach yield a more redundant (and hence, robust) system, but also allows different control approaches that, when hybridized with the traditional control strategies, provide better measures of performance.

In order to facilitate the design and analysis of the control strategies for combined maneuvers, this thesis proposed discrete analogs to, and a refinement of, Swaroop's string stability definitions. Moreover, a guarantee was also provided for Lyapunov-like stability of a special class of MIMO systems under approximate control(s). The string stability definitions were utilized to quantify the margin of stability available for the entire platoon under the hybrid longitudinal and lateral schemes. Conversely, the second result ensured

to the stability of the individual vehicle under approximate control. The sufficient conditions allowed the use of any number of numerical methods to compute the control, while assuring boundary-layer tracking performance.

However, due to vehicle and test track limitations, experimental validation of the points mentioned above remain open. As was noted in **chapter 2,** there does not currently exist a complete set of parameters for the Pontiac vehicle. In particular, the lack of engine maps for the Pontiac's 3.8L engine are especially troublesome. While experiments have been conducted using maps approximated from a Ford 5.0L engine, the resulting plant errors mask any performance difference between the combined controller and the independent lateral and longitudinal controllers. Additionally, the low speed nature of PATH's Richmond test track also make any comparisons difficult as the motion coupling become discernable only at higher speeds.

These limitations point to the need for further experimentation. Currently, PATH is in the process of outfitting the a new generation of test vehicles for combined lateral and longitudinal control. Obtaining the complete set of control and model parameters for these vehicles is a priority. In addition, PATH is also actively cultivating alternative test sites for high speed maneuvers. **As** these objectives are realized, it will be possible to conduct more meaningful experiments to corroborate the simulation model and to validate the control results.

In particular, we anticipate being able to conduct two-vehicle platoon experiments to verify the hybrid control strategies of **chapters 4** and **5.** The lone Pontiac vehicle is not adequate (as the follower vehicle) for hybrid longitudinal experiments since we require the lead vehicle to encounter the magnetic markers at a desired rate. Unfortunately, if a human were to drive the vehicle, sufficiently tight tracking cannot be guaranteed to ensure the sensor's picking up every marker. At high enough "miss rates," this could spell catastrophic failure for the longitudinal controller.

A further unresolved issue concerns the fact that two of the four control states are not currently measured, *i.e.* heading error and lateral velocity. However, by placing magnetic sensors at the front and rear of the vehicle, it is possible to estimate the heading error quantity, $\tilde{\psi}$. Experimental verification of this fact will be possible once magnetometers are mounted at the front and rear of the next-generation vehicles. The availability of this additional measurement should encourage more work in the nonlinear vehicles state estimation problem. For currently, one of the biggest obstacles to satisfactory controller implementation is the lack of adequate state estimates.

References

Ackermann, J., Sienel, W. "Robust Control for Automatic Steering," *Proceedings of 1990 American Control Conference,* San Diego, CA, pp 795-800, 1990.

Anderson, B., Moore, J., *Optimal Control, Linear Quadratic Methods,* Prentice-Hall, Inc., NJ, 1990.

Bakker, E., Nyborg, L., Pacejka, H. B. "Tyre Modelling for Use in Vehicle Dynamics Studies," SAE Technical Paper Series, no 870421, 1987.

Bakker, E., Pacejka, H. B. Lidner, L. "A New Tyre Model with an Application in Vehicle Dynamics Studies," SAE Transactions, *Journal of Pasenger Cars,* vol 98, no 890087, SAE Technical Paper, 1989.

Bender, J., Fenton, R. "On the Flow Capacity of Automated Highways," *Transportation Science,* vol 4, pp 52-63, 1970.

Butsuen T., Hedrick, J. K., "Optimal Semi-active suspension for Automotive Vehicles," *Advanced Autmotive Technologies,* Dsc-vol 13, ASME-WAM, 1989.

Callier, F., Desoer, C., *Linear System Theory,* Springer-Verlag, NY, 1991.

Caudill, R., Garrard, W. "Vehicle Follower Longitudinal Control for Automated Guideway Transit Vehicles," *ASME Journal of Dynamic Systems, Measurement and Control,* vol 99, no 4, 1977.

Caywood, W., Donnely, H., Rubinstein, N. "Guideline for Ride-Quality Specifications Based on Transpo '72 test data," Johns Hopkins University Applied Physics Laboratory, Urban Mass Transportation Administration, Office of Research and Development, Springfield, VA, available through the National Technical Information Service, 1977.

Choi, S. *Design of a Robust Controllerfor Automotive Engines: Theory and Experiment,* PhD Disertation, University of California, Berkeley, 1993.

Chiu, A., Stupp Jr., G., Brown Jr., S. "Vehicle Follower Control with Variable Gains for Short Headway Automated Guideway Transit Systems," *Journal of Dynamic Systems, Measurements and Control,* September 1977, pp 183-189.

Deseor, C., Vidyasagar, M., *Feedback System: Input-Output Properties,* Academic Press, 1975.

Dickmanns, E., Zapp, A. "Autonomous High Speed Road Vehicle Guidance by Computer Vision," *Proceedings of 10th IFAC World Congress,* Munich, 1987.

Fenton, R., Selim, I. "On the Optimal Design of an Automotive Lateral Controller," *ZEEE Transactions on Vehicle Technology,* vol 37, no 2, pp 108-113, May 1988.

Fenton, R., Bender, J. "A Study of Automatic Car Following," *IEEE Transactions on Vehicular Technology,* vol VT-18, no 3, Nov 1969.

Garrard, W.L., Kornhauser, **A.,** "Use of State Observers in the Optimal Feedback Control of Automated Transit Vehicles," *ASME Journal of Dynamic Systems, Measurement and Control,* vol 95, no 2, pp 220-227, 1973.

Gerdes, C., Maciuca, D., Devlin, P., Hedrick, J. K. "Brake System Modelling for IVHS Longitudinal Control," *Advances in Robust and Nonlinear Control,* DSC-vol 53, pp 119-126, ASME Winter Annual Meeting, 1993.

Green, J., and Hedrick, J. K. "Nonlinear Torque Control of Gasoline Engines," *Proceedings of 1990 American Controls Conference,* San Diego, CA, 1990.

Guldner, J.,Tan, H.S., Patwardhan, **S.** "Analysis of Automatic Steering Control for Highway Vehicles with Look-down Reference Systems," *Vehicle System Dynamics: International Journal of Vehicle Mechanics and Mobility,* Vol26 No 4, pp. 243-269, 1996.

Guldner, J., Utkin, V., Ackerman, J. "A Sliding Mode Control Approach to Automatic Car Steering," *Proceedings of 1994 American Controls Conference,* Baltimore, MD, pp 1969-1973, 1994.

Hedrick, J. K., Garg, V. *Failure Detection and Fault Tolerant Controller Design for Vehicle Control,* University of California, Berkeley: Institute of Transportation Studies, California PATH Program, UCB-ITS-PRR-93-09, 1993.

Hedrick, J. K., Garg, V., Gerdes, J., Maciuca, D., Swarop, D. *Longitudinal Control Development for IVHS Fully Automated and Semi-Automated Systems: Phase 11,* California PATH Research Report,UCB-ITS-PRR-96-1, 1996.

Hedrick, J. K., McMahon, D., Narendran, V., Swaroop, D. "Longitudinal Vehicle Controller Design for IVHS Systems," *Proceedings of the 1991 American Control Conference,* Boston, MA, 1991.

Hedrick, J. K., McMahon, D., Swaroop, D., Garg, V., Gerdes, J., Maciuca, D., Blackman, T., Yip, P. *Longitudinal Control Development for ZVHS Fully Automated and Semi-Automated Systems-Phase I,* California PATH Research Report,UCB-ITS-PRR-95-04, 199.5.

Hessburg, T., Peng, H., Zhang, W.B., Arai, A., Tomizuka, M. *Experimental Results of Fuzzy Logic Control for Lateral Vehicle Guidance,* University of California, Berkeley: Institute of Transportation Studies, California PATH Program, UCB-ITS-PRR-94-03, 1994.

Ioannou, P., Ahmed-Zaid, F., Xu, Z. "**A** Time Headway Autonomous Intelligent Cruise Control," PATH Working Paper, UCB-ITS-PWP-94-07, 1994.

Isidori, **A.** *Nonlinear Control Systems,* Springer-Verlag, 1989.

Kanayama, Y., Hartman, B.I. "Smooth Local Path Planning for Autonomous Vehicles," *1989 IEEE International Conference on Robotics and Automation,* vol 3, pp 1265-70, 1989.

Kanayama, Y., Miyake, N., "Trajectory Generation for Mobile Robots," *Proceedings of 3rd International Symposium on Robotics Research,* Gouvieux, France, pp 333-340, 1985.

Koller, D., Luong, T., Malik, J. *Binocular Stereopsis and Lune Marker Flow for Vehicle Navigation: Lateral and Longitudinal Control,* University of California, Berkeley: Instituite of Transportation Studies, California PATH Program, UCB-ITS-PRR-94-804, 1994.

Love, D., Tomizuka, M. *Vehicle Longitudinal Control Using Discrete Markers,* University of California, Berkeley: Institute of Transportation Studies, California PATH Program, UCB-ITS-PRR-94-28, 1994.

Mayhan, R., Bishel, R. "A Two-frequency Radar for Vehicle Automatic Lateral Control," *IEEE Transactions on Vehicle Technology,* vol VT-31, Feb 1982.

McMahon, D., Narendran, V. K., Swaroop, D., Hedrick, J. K., Chang, K. **S.,** Devlin, P. "Longitudinal Vehicle Controllers for IVHS: Theory and Experiment," *Proceedings of the 1992 American Control Conference,* Chicago, 1992.

Moskwa, J., Hedrick J. K., "Sliding Mode Control of Automotive Engines," *Proceedings of 1989 American Controls Conference,* Pittsburg, PA, **pp** 1040-1045, 1989.

Narendran, V. K., *Transportation Maneuvers in Intelligent Vehicle Highway System,* Ph.D. Dissertation. University of California, Berkeley, 1994.

Narendran, V. K., Hedrick, J. K. "Autonomous Lateral Control," *Vehicle System Dynamics,* Jun 1994.

Nashman, M., Schneiderman, H. "Real-Time Visual Processing for Autonomous Driving," *Proceedings of the Intelligent Vehicle 1993 Symposium,* Tokyo, Japan, 1993.

Nelson, W. "Continuous-Curvature Path for Autonomous Vehicles," *1989 IEEE International Conference on Robotics and Automation,* pp. 1260-4, May 1989.

Nelson, W., Cox, I., "Local Path Control for an Autonomous Vehicle," *International Conference on Robotics and Automation,* Philadelphia, PA, pp 1504-1510

Nijmeijer, H., Van der Schaft, J. *Nonlinear Dynamical Control Systems,* Springer-Verlag, 1990.

Peng, H. *Vehicle Lateral Control for Highway Automation,* PhD Dissertation, University of California, Berkeley, 1992.

Peng, H., Tomizuka, M. "New Tire Model for the Toyota Celica Test Vehicle," PATH internal report, Apr 1991

Peng, H., Tomizuka, M. "Vehicle Lateral Control for Highway Automation," *Proceedings of the 1994 American Control Conference,* San Diego, CA, pp 788-794, May 1990.

Peng, H. Tomizuka, M. "Preview Control for Vehicle Lateral Guidance in Highway Automation," *Proceedings of the 1991 American Controls Conference,* pp 3090-3095, 1991.

Pham, H. *Combined Lateral and Longitudinal Control of Vehicles for the Automated Highway System,* PhD Dissertation, University of California, Berkeley, 1996.

Pham, H., Hedrick, J. K., Tomizuka, M. "Combined Lateral and Longitudinal Control of Vehicles for IVHS," *Proceedings of the 1994 American Control Conference,* Baltimore, MD, pp 1205-1206, June 1994.

Shladover, S. "Dynamic Entrainment of Automated Guidway Transit Vehicles," *High Speed Ground Transportation Journal,* vol 12, no 3, pp 87-113, 1978.

Shladover, S. "Vehicle-follower Control for Dynamic Entrainment of Automated Guideway Transit Vehicles," *Transactions of ASME,* vol 101, pp 314-320, Dec 1979.

Slotine, J.E., Li, W. *Applied Nonlinear Control,* Prentice-Hall, NJ, 1991.

Swaroop, D. *Stability of Interconnected Systems,* PhD Disertation, University of California, Berkeley, 1994.

Tomizuka, M., Hedrick, J.K. "Automated Vehicle Control for IVHS Systems," IFAC Conference, Sydney, Australia, 1993.

Tomizuka, M., Hedrick, J. K., Pham, H. *Integrated Maneuvering Control for Automated Highway Systems,* University of California, Berkeley: Institute of Transportation Studies, California PATH Program, UCB-ITS-PRR-95-4, 1995.

Tseng, E. *A Methodology for Optimizing Semi-Active Suspensions for Automotive Applications,* PhD Disertation, University of California, 1991.

Whitney, D. E., Tomizuka, M. "Normal and Emergency Control of a String of Vehicles by Fixed Reference Sampled-Data Control," *IEEE Transactions on Vehiclar Technology,* vol VT-21, no 4, pp 128-138, 1972.

Yokoyama, T., Tachibana, A., Suzuki, T., Inoue, H. "Automated Vehicle System Using Both a Computer Vision and Magnetic Field Sensors," *Proceedings of the Intelligent Vehicle 1993 Symposium,* Tokyo, Japan, 1993.

Utkin, V. "Variable Structure Systems with Sliding Modes," *IEEE Transactions on Automatic Control,* vol AC-22, pp 212-222, 1977.

Zhang, W., Parsons, R., West, T. "An Intelligent Roadway Reference System for Vehicle Lateral Guidance/Control," *Proceedings of the 1990 American Control Conference,* pp 281-286.

Zhao, G., Yuta, S. "Obstacle Detection by Vision System for an Autonomous Vehicle," *Proceedings of the Intelligent Vehicle 1993 Symposium,* Tokyo, Japan, 1993.

Appendix A. Vehicle model parameters

variable	*description*		*value*	
I_x	moment of inertia about x-axis		479.6	[kg-m^2]
I_y	moment of inertia about y-axis		2549.3	[kg-m^2]
I_z	moment of inertia about z-axis		2782.7	[kg-m^2]
J_{eng}	engine inertia		0.2630	[kg-m^2]
$J_{gear}(i)$	i^{th} gear inertia	(1)	0.07582	[kg-m^2]
		(2)	0.08202	
		(3)	0.11388	
		(4)	0.13150	
J_w	wheel inertia		1.2825	[kg-m^2]
m	vehicle mass		1573	[kg]
h_0	vertical distance to c.g		0.487	[m]
h_2	vertical distance from c.g. to roll center		0.30	[m]
h_4	vertical distance from c.g. to pitch center		0.25	[m]
h_5	long. distance from c.g. to pitch center		0.10	[m]
l_1	distance from c.g. to front axle		1.034	[m]
l_2	distance from c.g. to rear axle		1.491	[m]
s_b	track of vehicle		1.450	[m]
r_w	wheel radius		,3044	[m]
C_{sf}	cornering stiffness of front tire		66366	[N]
C_{sr}	cornering stiffness of rear tire		52812	[N]
F_{roll}	total tire rolling resistance		274.7	[N]
MAX	maximum manifold intake airflow		684.109	
T_{man}	manifold temperature		310.93	[C^o]
V_{man}	manifold volume		0.00447	[L]
c_x	wind drag coefficient x-dir		.45	
c_y	wind drag coefficient y-dir		2.1	
$r_{gear}(i)$	i^{th} gear ratio	(1)	0.4167	
		(2)	0.6817	
		(3)	1.0000	
		(4)	1.4993	

Appendix B. Tire model (Bakker-Pacjeka)

Fitted on Yokohoma P205/60R1487H steel-belted radials

(C1) $$F_x = D_x \sin(C_x \tan^{-1}(B_x\phi_x)) + S_{vx}$$

(C2) $$F, = D, \sin(C_y \tan^{-1}(B_y\phi_y)) + S_{vy}$$

(C3) $$\phi_x = (1\text{-}E_x)(i_s + S_{hx}) + \frac{E_x}{B_x}\tan^{-1}(B_x(i_s + S_{hx}))$$

(C4) $$\phi_y = (1 - E_y)(\nu + S_{hy}) + \frac{E_y}{B_y}\tan^{-1}(B_y(\nu + S_{hy}))$$

traction ($i_x > 0$)

$$B, = 22 + \frac{F_z - 1940}{645}$$

$$C, = 1.35 - \frac{F, - 1940}{16125}$$

$$D_x = 1750 + \frac{F, - 1940}{.956}$$

$$E_x = -3.6$$

$$S_{hx} = 0$$

$$S_{vx} = 0$$

braking ($i_x < 0$)

$$B, = 22 + \frac{F, - 1940}{430}$$

$$C, = 1.35 - \frac{F_z - 1940}{16125}$$

$$D_x = 1750 + \frac{F_z - 1940}{.956}$$

$$E, = 0.1$$

$$S_{hx} = 0$$

$$S_{,,} = 0$$

$$B_y = 0.22 + \frac{5200 - F_z}{40000}$$

$$C_Y = 1.26 + \frac{F_z - 5200}{32750}$$

$$D_y = -0.00003F_z^2 + 1.0096F_z - 22.73$$

$$E_x = -1.6$$

$$S_{hy} = 0$$

$$S_{,,} = 0$$